Revision 2

Re-examination of *vesbine* in vanadate-rich sublimate-related associations of Vesuvius (Italy): mineralogical features and origin

Annamaria Pellino[1], Giuseppina Balassone[1,2,3,*], Isabel Abad[4], Angela Altomare[5], Fabio Bellatreccia[6], Piergiulio Cappelletti[1,2,7], Aurelia Falcicchio[5], Nicola Mondillo[1,8], Richard Herrington[8], Cristiana Isè[1], Carmela Petti[7], Mike Rumsey[9]

[1] Department of Earth Science, Environment and Resources (DiSTAR), University of Naples Federico II, Via Cintia, 26, Naples I-80126, Italy

[2] Center for Research on Archaeometry and Conservation Science (CRACS), University of Naples Federico II, Via Cintia, 26, Naples I-80126, University of Sannio, Via dei Mulini 73, Benevento I-82100, Italy

[3] National Institute of Geophysics and Volcanology (INGV), Vesuvius Observatory, Via Diocleziano I-80124 Naples, Italy

[4] Department of Geology and CEACTEMA, University of Jaén, Campus Las Lagunillas s/n, 23071 Jaén, Spain

[5] Institute of Crystallography-CNR, Via G. Amendola 122/o, 70126 Bari, Italy

[6] Department of Science, University Roma Tre, Largo S. Leonardo Murialdo 1, I-00146, Roma, Italy

[7] Royal Mineralogical Museum, Centre of Natural and Physical Sciences Museums, University of Naples Federico II, Via Mezzocannone 8, Naples I-80134, Italy

[8] Earth Sciences Department, Natural History Museum, Cromwell Road, London, SW7 5BD, UK

[9] Mineral and Planetary Science Curation, Science Department, Natural History Museum, Cromwell Road, London, SW7 5BD, UK

* Corresponding author: balasson@unina.it

RUNNING TITLE: Vanadate-rich association of Vesuvius

ABSTRACT

A set of 23 *vesbine*-bearing samples from Vesuvius volcano (Italy), preserved in the collection of the Royal Mineralogical Museum of Naples, University Federico II (RMMN), have been investigated to identify the mineral assemblages and their mode of formation. In the late nineteenth century, fumarole-related yellow patinas coating some historical lavas from Vesuvius were believed by Scacchi to contain a new element, vesbium, similar to vanadium in a mineral he called *vesbine*. Subsequent studies rejected vesbium and showed that *vesbine* was a poorly-defined mixture of copper vanadates and halides. The *vesbine* samples studied here consist of yellowish to yellow-green-blue encrustations on Vesuvius lavas and have been analyzed by combined optical microscopy, SEM-EDS, XRPD, FTIR and TEM-HRTEM-EDS. Results reveal complex mineral associations, including vanadates, halides, carbonates, oxides, silicates, tungstates/molybdates and sulfates. The vanadates correspond to mottramite, volborthite and vanadinite; subordinate amounts of descloizite were detected by XRPD and FTIR investigations. Several different additional non-essential elements have been detected in the vanadates, including Mn, Zn and As. The occurrence of wulfenite- and stolzite-rich phases indicates the presence of Mo and W, along with Pb, in the mineralizing fluids. Mn-rich phases, commonly in mixtures with silicates and vanadates, were also observed. These minerals are formed by a combination of different processes, including rock-fluid interactions, gas-water interactions, and alteration/oxidation of primary fumarolic minerals. Temperatures for the depositions of the vanadates-bearing assemblages are interpreted to be in the range of 100 to 400 °C.

Keywords: vanadates, *vesbine*, volborthite, mottramite, vanadinite, copper-bearing minerals, fumaroles, Vesuvius

INTRODUCTION

In 1879, Arcangelo Scacchi (at that time Director of the Royal Mineralogical Museum of Naples, University Federico II, henceforth RMMN) reported the discovery of a new element, similar to vanadium, in tiny yellow sublimate-related crusts (*vesbine*) coating some lavas, that he attributed to the 1631 AD eruptive event of Vesuvius volcano (Southern Italy). However, as reported by Russo and Punzo (2004), Russo et al. (2011), and Mottana (1998), the *vesbine* occurrences should instead be attributed to medieval fumarolic activity. Scacchi provisionally named this new element *vesbium* (from the Latin name of Vesuvius) and *vesbine* the mineral (containing *vesbium* and aluminum), of which the yellow crusts were formed (Scacchi, 1879, 1880a, 1880b, 1882). Due to the rarity and the small quantity of these crusts, and the difficulty of obtaining pure samples, no further study was carried out on *vesbine* for several years. Then, Zambonini (1910) and Zambonini and Carobbi (1927) showed the connection of *vesbium* with vanadium, identifying *vesbine* as a hydrated "cuprodescloizite" (see also Mottana, 1998). De Luise (1914) also analyzed *vesbine* samples and interpreted them as a mixture of lead-zinc vanadate [descloizite, $PbZn(VO_4)(OH)$] and copper vanadate [volborthite, $Cu_3V_2O_7(OH)_2 \cdot 2H_2O$], with probably an undetermined oxychloride of copper. Zambonini and Carobbi (1927) detected minor elements in the *vesbine*, including REE (La, Ce, Nd, Dy and Y), W, Mn, Co, Ti, Ta, Nb, and Al (Russo and Punzo, 2004).

Russo and Punzo (2004) reported that *vesbine*-bearing crusts were more likely composed of a mixture of vanadates, corresponding to volborthite, mottramite [$PbCu(VO_4)(OH)$], descloizite, and vesignieite [$Cu_3Ba(VO_4)_2(OH)_2$], and associated with atacamite [$Cu_2Cl(OH)_3$], azurite [$Cu_3(CO_3)_2(OH)_2$], and hausmannite [$Mn^{2+}Mn^{3+}{}_2O_4$]. Recent investigations (Balassone et al., 2019) on a few samples from the Vesuvian Collection of the RMMN confirmed that the *vesbine* samples correspond to complex mixtures of vanadates, mainly mottramite and volborthite, with lesser vanadinite [$Pb_5(VO_4)_3Cl$]. Variable amounts of wulfenite ($PbMoO_4$), atacamite, tenorite (CuO), chrysocolla [$(Cu_{2-x}Al_x)H_{2-x}Si_2O_5(OH)_4 \cdot nH_2O$] and likely starovaite [$KCu_5O(VO_4)_3$] were additionally identified. This brought the total number of mineral species relevant to the composition of the *vesbine* crusts to 12.

Vanadates described in volcanic hydrothermal environments are restricted to very few worldwide occurrences and are represented by both anhydrous and $OH \pm H_2O$-bearing phases. Most anhydrous vanadates in nature are found in oxidizing-type volcanic fumaroles (Koshlyakova et al., 2022). They are known only in active volcanoes, Izalco in El Salvador (Hughes and Stoiber, 1985), and Tolbachik and Bezymyannyi, both in Kamchatka, Russia (Koshlyakova et al., 2022; Pekov et al., 2013, 2015 2020a,b, 2022a,b, 2023; Shchipalkina et al., 2020). The greatest number of fumarolic vanadates is known from the Tolbachik volcano and most of them contain Cu^{2+} as the species defining metal cation (Pekov et al., 2015, 2018). Vanadium occurring as a native element was found in sublimates from high-temperature fumaroles of the Colima volcano (Mexico), in association with the rare colimaite (K_3VS_4) and shcherbinaite (V_2O_5), formed at temperatures of 550–680 °C (Ostrooumov and Taran, 2016).

In this study, we report a detailed characterization of the V-bearing mineral assemblages on old *vesbine* samples from the Vesuvius volcano kept in the RMMN. The samples are mainly composed of fumarole-related yellow-greenish patinas and encrustations deposited on the surface of lavas from

activity of Vesuvius over the last several centuries. The purpose of the characterization is to investigate the genesis of this assemblage.

GEOLOGICAL AND VOLCANOLOGICAL SETTING

Vesuvius has been active for about 40,000 years with numerous eruptions in recorded historical times. The volcano is located at the southern end of the Roman Magmatic Province, in the Campanian volcanic district (e.g., Conticelli et al., 2011), and the volcanism in this broader area started about 400 ka BP (Di Renzo et al., 2007, and references therein).

The Somma-Vesuvius activity displayed a wide variety of styles, from high-energy Plinian eruptions to lower-energy sub-Plinian and Strombolian activity and lava emission (Santacroce et al., 2008, and references therein). Between 22 ka BP and 1944 AD, the eruptive activity has been divided into four phases (Cioni, 2000; Cioni et al., 1999, 2008, 2013): first phase, with the formation of the volcanic apparatus of Somma; second phase, with Plinian and sub-Plinian eruptions (*Pomici di Base, Pomici Verdoline, Mercato, Avellino and Pompeii*); third phase, with sub-Plinian eruptions (i.e. *Pollena*) which ended with the 1631 eruption; fourth phase between the eruption of 1631 and that of 1944 AD, which constructed the current form of the volcanic edifice of Somma-Vesuvius.

After the well-known 79 AD (*Pompeii*) eruption, which destroyed the towns of Pompeii and Ercolano, the Vesuvius cone began to form within the caldera during periods of open conduit activity (Sbrana et al., 2020) which occurred during the I-III century (*Santa Maria* Cycle; Cioni et al., 2013), followed by the sub-Plinian 472 AD *Pollena* eruption, and in the V-VIII and X-XII centuries (*San Pietro* Cycle and *Villa Inglese* lava flows) that preceded the sub-Plinian event of 1631 AD (Sbrana et al., 2020). After this major eruption, the volcano entered a period of semi-persistent open-conduit

activity, characterized by a series of low-energy effusive and explosive eruptions, alternating with short rest periods. Each of these periods of activity ends with a high-energy eruption. Since the last eruption of 1944, Vesuvius has been quiescent.

As reported by Del Pezzo et al. (2013), immediately after the last eruption, volcanic activity was characterized by high-temperature fumaroles (600-800°C) as, at that time, the system hosted volcanic vapors. Subsequently, by 1964, the temperature of the fumaroles had dropped down to 290°C. Measurements carried out after 1975 showed temperatures in the range 220-240°C, and the present values are around 95°C. Between 1960 and 1970, the cold groundwaters present inside the adjacent carbonate-rich geological units probably began to enter the hot zones of the volcanic conduits cooling the system while increasing fluid pressure.

Vesuvius fumarolic activity and mineralogy

Between the end of the XIX century and the beginning of the XXI century, systematic research on the relationships between the temperature of the fumarolic gases and the chemistry of the vesuvian fumarolic mineralogy was carried out by Deville (1855), on the 1855 eruption, and Lacroix (1906, 1907), while Russo and Campostrini (2008) investigated the 1906 eruption and other historical eruptions. As reported by Pelloux (1927), Lacroix (1906, 1907) classified older Vesuvian fumaroles in four different types: high-temperature "dry" fumaroles, with halite, sylvite, thenardite $Na_2(SO_4)$, Na-K carbonates, aphthitalite $K_3Na(SO_4)_2$, sulfides, Cu-oxides, and chlorides as alteration (T > 300-400 °C); medium-temperature "acid" fumaroles, characterized by Fe, Mg, Al, and Mn chlorides, sulfur, and realgar (T = 100-300 °C); fumaroles with salammoniac with ammonium sulfate and fluoride (T ~ 300 °C); and low-temperature fumarole producing sulfuric acid and steam with sulfur, gypsum, sassolite, K-Al-Fe sulfates, and opal (T ~ 100 °C).

Balić-Žunić et al. (2016) classified the fumaroles from active European volcanoes (including Vesuvius) in three categories: high-temperature (HT) fumarole, >400 °C, (characteristic minerals: halite; thenardite, aphthitalite; anhydrite); medium-temperature (MT) fumarole, 200–400°C (characteristic minerals: type A, salammoniac, and other ammonium minerals; type B, metal chlorides; type C, ralstonite, and other aluminofluorides); low-temperature (LT) fumarole, <200°C (characteristic minerals: sassolite; gypsum; alunogen; sulfur). HT fumaroles appear with the eruption of the volcano and are short lived. MT and LT fumaroles might be active at the same time as the HT fumaroles, but at different places in the system where fumarolic gases travelled further and have cooled and/or been diluted by mixing with the atmosphere before they came to the surface. MT fumaroles prevail in the period of recession after the paroxysm while the shallow intruded magma cools down, or the degassing surface of the magma retreats to greater depths and last roughly for decades, maybe centuries. LT fumaroles are the only ones present in quiescent periods and have a deep thermal source and may eventually transform to a *solfatara* (*mofeta*), if the volcanic cycle is finished or very much prolonged (Balić-Žunić et al., 2016).

According to Pekov et al. (2020a, and references therein), mineral-forming fumaroles can be divided into two types according to the oxygen fugacity of the hot gas: (i) reducing, with gases only of volcanic origin, and (ii) oxidizing, where primary volcanic gas is mixed with atmospheric air before mineral formation. Most fumarole minerals crystallize through desublimation (such minerals are usually called volcanic sublimates). Mineral assemblages (first, high-temperature ones) formed in reducing- and oxidizing-type fumaroles differ considerably as elements combine in different oxidation states. Sulfur, abundant in almost all volcanic sublimates, can be considered the main indicator of the oxidative potential in a fumarolic system forming high-temperature sulfides in reducing-type and sulfates in oxidizing-type fumaroles.

Currently, the volcanic-hydrothermal activity of Vesuvius is relatively low, and fumarolic vents are situated on the crater rim and at its bottom. According to Caliro et al. (2011), the activity is characterized by (a) widespread fumarolic emissions, accompanied by diffuse soil CO_2 degassing in the crater area (Frondini et al., 2004), (b) CO_2-rich groundwater on the southern flank of Vesuvius and in the adjacent plain and (c) seismic activity with epicenters inside the crater. The fumaroles located on and inside the crater rim are characterized by fluids rich in atmospheric gases with relatively low temperatures (60 to 75 °C, Chiodini et al., 2001). Fumaroles from the crater bottom have a composition that shows H_2O and CO_2 as the major components, followed by H_2, H_2S, N_2, CH_4, CO and He (in order of decreasing content), and discharge temperature of about 95 °C, i.e., the condensation temperature of fumarolic fluids at the crater altitude (P_{atm} = 0.91 bar) (Caliro et al., 2011). According to Chiodini et al. (2001), the presence of significant contents of CH_4, together with NH_3 among other minor components, indicates an origin of these fluids related to a hydrothermal system located below the crater area.

Minerals in fumaroles are formed either as direct volcanic sublimates or from the reaction between gas and the material of the walls of fumarole conduits (gas-rock interaction), as well as other fumarolic encrustations. Many minerals were formed during the cooling (degassing) of the lava and the scoriae (Coradossi, 1980; Africano et al., 2002; Balić-Žunić et al., 2016). Sometimes it is difficult to determine whether a given sample is a true product of sublimation or is produced by secondary changes.

Among the European fumarole localities, Vesuvius and Vulcano (Sicily) are the two volcanoes with the richest mineralogy (Balić-Žunić et al., 2016). This is because of the exceptional enrichment of particular metals, semi-metals, and non-metals in their emanations: Cu, Pb, Cr, Mn, Ni, B, Tl, As, Se have been detected in Vesuvius. The presence of these elements however is not the only reason for the diversity in the mineralogy of the fumaroles (Balić-Žunić et al., 2016).

A pioneering paper on base metal enrichment in volcanic sublimates and secondary alteration products at Vesuvius was published by Angus and Davis (1976). These authors analyzed the sublimates and/or alteration products on the Johnston-Lavis collection in London (collected over the period 1880-1910), and the base metal concentrations (Cu, Pb, Zn) in aphthitalite and *natrikalite* (a disused term for a halite-sylvite mixture). They hypothesized, based on the observation of direct sublimation of tenorite and Pb oxides along with halite from high-temperature gases escaping from fissures in the 1872 lava, that the process leading to the Cu and Pb enrichment in fumaroles may have been vapor phase transport as volatile chlorides, which were decomposed with increasing oxygen fugacity and ultimately deposited as oxides.

THE SAMPLES

For this study, 23 *vesbine* samples (Table 1) have been selected from the historical Vesuvian collection of the RMMN, where vanadium minerals occur mainly as thin yellow/green patinas or encrustations on lavas of the relatively recent activity of Somma-Vesuvius. These samples have never been studied before, because they belong to a "working" collection of Arcangelo Scacchi (and inherited by his son, Eugenio Scacchi). Only ten of the samples have labels detailing the prevailing mineral(s), occurrence, eruption, and the acquisition year, the others give just catalogue ID numbers.

When present, the original museum labels and the old literature (Scacchi, 1879, 1880a, 1880b, 1882), indicate that the geological provenance of the *vesbine*-bearing lavas of the RMMN was considered to be the "1631 lavas", but Scacchi (1880a, 1882, 1890) commonly avoided reporting their exact sampling location. Some possible provenances of the Scacchi's samples (i.e. *Villa Inglese* at Boscoreale, *Camaldoli della Torre*, *Scogli della Scala* at Torre del Greco, and *Cupa dei Monti* at

Ercolano) have been hypothesized and reported in the literature (Mottana, 1998, and references therein; Russo and Punzo, 2004), however, lavas occurring in these sites do not belong to the 1631 AD activity (Mottana, 1998, and references therein). These studies suggest that *vesbine*-bearing samples are more likely related to the medieval activity of Vesuvius (968-1037 AD) (Rolandi et al., 1998). Further evidence for the earlier origin is that according to some authors (Rosi et al.,1993; Principe et al., 2004), the 1631 AD activity can be classified as a sub-Plinian eruption and did not produce lava flows, but pumice fall deposits, pyroclastic surges, and lahars. It is interesting to note that Russo and Punzo (2004) also reported another occurrence for some *vesbine*-like samples on lavas from the 1868 AD activity at Terzigno.

The vanadates and associated samples studied herein occur from very thin films to irregular encrustations with variable thickness. They may be dispersed across the lava surfaces and appear fine-grained or amorphous in appearance, in some cases they can form concentric aggregates or zoned micrometric rosettes. The samples selected for this study were those visually richer in *vesbine*-bearing assemblages. One group of specimens is characterized by a deep yellow, thin, and powdery patina while other samples have a strongly zoned texture at the macroscopic scale with yellow, green, turquoise, and deep blue patches or banding with occasional small, rounded more crystalline aggregates (Fig. 1).

ANALYTICAL METHODS

Due to the nature of the *vesbine* occurrence, the separation of fragments and powders from the hosting lavas of the RMMN samples (Table 1, Fig. 1) was difficult. To obtain polished thin sections containing *vesbine*-rich crusts (at least at a first macro-to-mesoscopic evaluation), various sub-samples

were selected from each sample; these were prepared by soaking them in Buehler Epokwich™ FC epoxy resin and placing them in different orientations, then carefully polished.

Thin sections were studied by means of polarizing Optical Microscopy (OM) using a transmitted light Laborlux 12 POL polarizing microscope equipped with a Carl Zeiss Axiocam 105 color (5-megapixel resolution) and Carl Zeiss ZEN digital imaging analysis software.

SEM observations were carried out with a JEOL JSM5310 at the Dipartimento di Scienze della Terra, dell'Ambiente e delle Risorse (DiSTAR), Università degli Studi di Napoli Federico II, Italy. Analytical conditions were the following: working distance of 20 mm, and 15 kV voltage. EDS microanalyses were carried out with an INCA X-stream processor and Inca software v. 4.08 (Oxford Instruments detector). Standards used were anorthoclase (Si, Al, Na), microcline (K), diopside (Ca), olivine (Mg), fayalite (Fe), rutile (Ti), barite (Ba), strontianite (Sr), eskolaite (Cr), rhodonite (Mn), pyrite (S), copper (Cu), sphalerite (Zn), galena (Pb), silver (Ag), arsenopyrite (As), apatite (P), sylvite (Cl), vanadium (V). The error is around 1% for major elements and about 3% for trace ones. SEM observations on four samples (P9, P18-g, 902R, 911R-g) were also carried out at the Imaging and Analysis Centre, Core Research Laboratories of the Natural History Museum of London (UK) (henceforth NHM) with a variable pressure Zeiss EVO 15LS instrument with Oxford Aztec software 5.0. Analytical conditions were 10 mm working distance and 20 kV acceleration voltage and a Co standard.

Electron microprobe analyses (EPMA) utilizing wavelength dispersive spectroscopy (WDS) were carried out at NHM (London), using a Cameca SX100 with five wavelength dispersive X-ray spectrometers. Reference standards used for quantitative microanalyses were jadeite (Na), fayalite (Si, Fe), scandium phosphate (P), corundum (Al), forsterite (Mg), wollastonite (Ca), $MnTiO_3$ (Mn, Ti), orthoclase (K), halite (Cl), barite (Ba, S), eskolaite (Cr), vanadinite (V), CuO (Cu), sphalerite (Zn),

NiAs (As), molybdenum (Mo), tungsten (W), Pb glass (Pb); the operating conditions were 20 keV and 10 nA with a 20 μm beam diameter.

A selection of powders for X-ray diffraction and infrared spectroscopy was obtained by gently scratching the crusts, then trying to discard impure fragments (lava-contaminated) as much as possible using a stereomicroscope. X-ray powder diffraction (XRPD) data were collected at the Institute of Crystallography of CNR of Bari (IC-CNR), Italy, at room temperature using an automated Rigaku RINT2500 rotating anode laboratory diffractometer (50 kV, 200 mA) equipped with the silicon strip Rigaku D/teX Ultra detector.

An asymmetric Johansson Ge (111) crystal was used to select the monochromatic Cu Kα1 radiation (λ= 1.54056 Å). Measurement was executed in a transmission mode by introducing the sample in a glass capillary (0.5 mm diameter), which was mounted on the axis of the diffractometer. To reduce the effect of possible preferred orientation, the capillary was rotated during the measurement to improve the randomization of the orientations of the individual crystallites. Qualitative phase analysis was carried out through the software QUALX2.0 (Altomare et al., 2015), using the commercial PDF-2 database (ICDD, 2003) and the free POW_COD database. It is worth noting that the interpretation of the powder diffraction patterns is not straightforward due to their complexity having significant peak overlap.

For the morphological and chemical characterization at the nanometer scale, selected samples were prepared for transmission electron microscopy (TEM) analysis. Samples were prepared using an Au grid surface coated in a perforated formvar resin from a dispersion of finely ground sample particles, in alcohol. The monomineralic character of each grain was demonstrated by its electron diffraction pattern, confirming the existence of a single network and, therefore, a single crystalline phase. The TEM study was carried out at the Centro de Instrumentación Cientifica (CIC) of the Universidad de Granada, Spain, with the HAADF Thermo Fisher Scientific TALOS F200X microscope

operated at 200 kV and with a point-to-point resolution of 0.12 nm in the TEM mode and 0.19 nm in the STEM mode. The mineralogical features were also assessed by combining TEM with high-resolution TEM (HRTEM), scanning transmission electron microscopy (STEM), high-angle annular dark field (HAADF) and selected-area electron diffraction patterns (SAED). The nanoscale chemical characterization of minerals and the compositional maps were carried out in STEM mode through AEM-EDS (energy dispersive X-ray spectroscopy) using the Super-X system.

Powder Fourier Transform Infrared Spectroscopy (FT-IR) data of selected samples were collected at the Laboratorio di Spettroscopia Infrarossa, Department of Science, Roma Tre University, Italy, using a Nicolet iS50 FTIR spectrometer equipped with a DTGS detector and a KBr beamsplitter; the nominal resolution was 4 cm^{-1}, and 64 scans were averaged for each sample and for the background. Samples were prepared as pellets containing about 0.5 mg of powdered sample in 200 mg of KBr. For samples P9 and P18, it was possible to analyze two different fractions, separated based on their different color, and therefore named $P9_{yellow}$ and $P9_{green}$, $P18_{yellow}$ and $P18_{green}$.

RESULTS

OM, SEM-EDS, EPMA-WDS and XRPD

For the sake of simplicity, based on the macroscopic scale observation and combined mineralogical studies (Figs. 1 and 2, Table 2), the main mineral assemblages of the exhalative deposits can be sorted into two main groups: **Group I**, i.e. yellow encrustations (e.g. Fig. 1b,e,f), and **Group II**, i.e. yellow-green-blue encrustations (e.g. Fig. 1a,c,d,g,h). XRPD analysis was used in the necessary

cases to clarify the mineral nature of ambiguous identifications (see Fig. S1 for diffraction patterns of the investigated samples).

Group I

From the results of combined mineralogical analyses (Tables 1 and 2), Group I corresponds to a main assemblage with dominant volborthite, variably associated with mottramite±vanadinite± atacamite±stolzite-wulfenite. Only in sample 911R-g was volborthite not found. Chrysocolla, Mn-oxy-hydroxides, cerussite, gypsum and sylvite were also occasionally detected. Observed under OM (Fig. 2), samples of Group I show brilliant yellow aggregations of volborthite (Fig. 2d,g,h,i), which can include vanadinite crystals and gypsum occurring as euhedral needle-like crystals.

Overall, volborthite can occur in various habits, as rosettes, massive crusts or grape-like rounded aggregates of tiny elongated prismatic, platy to acicular individuals (Fig. 3a,b,d,e,f,k,l). In sample P2, volborthite forms tiny rosettes with a dark to light green core-to-rim zonation at a mesoscopic scale (see the inset in Fig. 3a), corresponding to the Vbo-1 and Vbo-2 of Fig. 3a. The chemical composition of these two zones indicates that the darker cores have slightly greater Cu compared to the lighter rims (Table S2). In sample 902R (Fig. 3c-f), volborthite can also grow on (amorphous?) rounded and banded aggregates, with variable V and Cu contents, as well as Mn (4-15 MnO wt.%) and detectable Si, Al, and Cl. In 911R-b tiny Pb-bearing (10-20% wt. oxide) microcrystals are observed forming roughly spherical clusters within volborthite with various habits (Fig. 3k); unfortunately, the size of the samples meant it was not possible to determine their composition accurately. In general, volborthite composition of Group I samples has low abundance of Si, Al, Mn, Zn, K and very small amounts of Ca, Fe, P and S (Table S2).

Mottramite occurs only in three samples, namely P8, 911R-g and 911R-b (Table 2); globular forms and granular microcrystals are typical (Fig. 3g-i). In sample 911R-g, mottramite crystallized after

vanadinite, partly replacing it (Fig. 3g-h). Chemically, mottramite shows almost constant Pb concentrations, but Cu and V vary and there can be significant impurity of Si, Al, and Ca (Table S3).

Vanadinite was identified in four samples (Table 2), forming rounded aggregates or euhedral hexagonal prisms (Fig. 3g,h). The chemical composition (Table S4) can contain small amounts of Cu, Si, Al, K and As.

Atacamite forms thin films in three samples (Fig. 1j, Table 2). In sample 911R-g (Fig. 3j), it can locally have significant amounts of MnO (up to 5.2 wt.%; see Discussion), as well as 1.1 wt.% MgO and FeO (Table S5).

Interestingly, a Cu-K-bearing vanadate, occurring in prismatic laths forming rounded and sheaf-like aggregates (Fig. 3m), is found in sample 911R-b; this phase, with a K content in the range of 5-8 wt.% (Table S6) was tentatively identified as starovaite-like but low totals, likely due to crystal size or hydration, preclude a more confident identification.

Very minor chrysocolla forms local cavity linings and may replace atacamite (Fig. 3j, Tables 2 and S6).

Wulfenite and stolzite (Tables 2 and S6) occur only rarely (Fig. 3i,m), and appear to precede the precipitation of volborthite and mottramite.

Group II

Group II is generally characterized in most samples by an atacamite-vanadinite-mottramite association, whereas volborthite occurs in half of the sample set (Table 2). Samples exhibit a strong zonation, both at hand-specimen (Fig. 1a,c,d,g,h) and at a micrometric scale compared to Group I (Figs. 2, 4 and 5), with a great mineralogical variety (Table 2). Regarding the main assemblages that form the distinctly coloured bands, the green parts consist of widespread atacamite (Fig. 2b,c,e,i,j,k,l; locally atacamite-related phases can occur, see below), with subordinate malachite (Fig. 2b,k,l) and

This is the peer-reviewed, final accepted version for American Mineralogist, published by the Mineralogical Society of America.
The published version is subject to change. Cite as Authors (Year) Title. American Mineralogist, in press.
DOI: https://doi.org/10.2138/am-2023-9126. http://www.minsocam.org/

chrysocolla; in sample 988R, another copper silicate was tentatively identified as dioptase, $CuSiO_3 \cdot H_2O$, due to the lack of Al in the EDS analyses (Table S6). However, the effective presence of this phase will have to be validated by further investigations. Azurite characterizes the blue parts, which when viewed using a microscope can be seen as forming minute turquoise blue bands and/or cockades (Table 2 and Fig. 2a,b). In the yellowish patches, vanadinite (almost ubiquitous) and mottramite can be associated with volborthite in half of the samples; these minerals form complex banded aggregations at a very fine scale (Fig. 2 e,k-r). Minor minerals detected only occasionally included Cu-oxides (tenorite, CuO, and cuprite, Cu_2O), as well as stolzite-wulfenite, anglesite ($PbSO_4$), gypsum and Fe-oxy-hydroxides (Table 2).

Under greater magnification, atacamite can be seen to form intergrowths with azurite (Fig. 4a), radiating clusters of crystals (Figs. 4b-d,i and 5c-i) or fine-grained and strongly zoned botryoidal concretions alternating and/or intergrowing with vanadates (Figs. 4h,k-o and 5j-o). It is worth mentioning that at least two generations of atacamite can be observed in sample P18, Mn-bearing rounded aggregates of atacamite-1 and Mn-free acicular atacamite-2, growing on atacamite-1 (Fig. 4i and Table S5). In this sample, several areas with tiny concentric bands (Fig. 4h) have compositions close to atacamite but containing significant amounts of PbO (5.3 wt.%), SiO_2 (2.3 wt.%), Al_2O_3 (1 wt.%), V_2O_5 (2.5 wt.%), and minor ZnO (1.0 wt.%) and MnO (0.8 wt.%). Other polymorphs of $Cu_2Cl(OH)_3$, botallackite and clinoatacamite have been detected by XRPD analyses in samples P9 and P18p, respectively, whereas paratacamite [$(Cu,Zn)_2Cl(OH)_3$] was potentially recorded in samples P18p, 912R, 984R, and 997R by XRPD (Table 2 and Fig. S1); however, since Zn is an essential component in paratacamite (Braithwaite et al., 2004) and it was not found in the sample that underwent EDS-WDS, an identification of paratacamite remains to be confirmed. On the whole, in the analyzed atacamite, significant amounts of Mn (up to 4.4 wt.% MnO), Pb (up to 3.6 wt.% PbO), Si (up to 1.8 wt.% SiO_2) and V (up to 1.4 wt.% V_2O_5) can be present (Table S5).

This is the peer-reviewed, final accepted version for American Mineralogist, published by the Mineralogical Society of America.
The published version is subject to change. Cite as Authors (Year) Title. American Mineralogist, in press.
DOI: https://doi.org/10.2138/am-2023-9126. http://www.minsocam.org/

Vanadinite was detected in most of the samples (Table 2). It occurs in diffuse clusters commonly at the nuclei of banded concretions (Fig. 4e-g,l-m). Among minor components, vanadinite may contain up to 5.7 wt.% CuO, 1.5 wt.% SiO_2, 2.8 wt.% CaO, and 1.4 wt.% As_2O_5 (Table S4). In sample 998R a composition with 6.5 wt.% P_2O_5 corresponds to ca. 46% of pyromorphite solid solution (Table S4).

Mottramite, quite common in this group, in the yellowish patinas of sample P18 typically surrounds vanadinite crystals (Fig. 4e-g). Mottramite can also occur in narrow and colloform bands with atacamite and vanadinite, as shown in sample 998R (Fig. 4l-o), or with atacamite and volborthite, as in sample 1002R (Fig. 5c-i). Chemical composition of mottramite (Table S3) shows up to 4.3 wt.% SiO_2, 3.8 wt.% Al_2O_3, 1.6 wt.% CaO and MnO, 1.6 wt.% ZnO, and 1.5 wt.% As_2O_5.

Volborthite in sample C26 (Fig. 4b) crystallized after cuprite and is followed by atacamite. Two generations, alternating with atacamite deposition, can be observed in sample P9, i.e. 'volborthite 1'→ atacamite → 'volborthite 2' (Fig. 4c,d). The volborthite varieties differ in their Mn content, 1.3 wt.% oxide in volborthite 1, and 3.7 wt.% oxide in volborthite 2 (Table S2). Significant concentrations of Mn (Table S2) are also detected in volborthite from other samples, such as 1000R-1 (1.5 wt.%) and 1002R (2.6-5.3 wt.%). In sample 1002R, volborthite typically forms fine-grained concentric layers and reniform bands with mottramite, as observed in Fig. 5c-e, j and the elemental EDS maps of Fig. 5f-i,k-o.

Malachite (Table 2) appears to be late in the paragenesis and partly replaces atacamite, as observed in Fig. 2k. It contains a maximum amount of 1.1 wt.% PbO (Table S7).

Azurite (Table 2) is almost stoichiometric, showing small contents of SiO_2 (up to 1.4 wt.%), ZnO (up to 1.2 wt.%) and MnO (up to 0.9 wt.%), and other minor elements (Table S7).

Minor occurrences of chrysocolla (Table 2) were observed as cavity linings in lava and formed after atacamite and vanadates (Fig. 4k,l). Trace amounts of Pb, Zn, Mn and Mg are detected (Table S6).

This is the peer-reviewed, final accepted version for American Mineralogist, published by the Mineralogical Society of America.
The published version is subject to change. Cite as Authors (Year) Title. American Mineralogist, in press.
DOI: https://doi.org/10.2138/am-2023-9126. http://www.minsocam.org/

Copper oxide minerals identified included cuprite confirmed by XRPD or EDS in samples C26 (Fig. 4b) and P9, and tenorite only in sample 998R by XRPD (Tables 2 and S6).

Stolzite-wulfenite phases occur as anhedral masses or euhedral crystals in some samples (Figs. 4h-k and 5b), showing evidence of at least two generations. Representative compositions are reported in Table S6.

Finally, in Group II, it is quite common to observe tiny bands and the inner parts of rounded concretions with compositions likely corresponding to complex mixtures of vanadates, chlorides, silicates, and phosphates that cannot be deconvoluted; as shown in sample 998R, the Si content is up to 18 wt.% (Fig. 4,l,p), and P up to 8 wt.% oxide (Fig. 4n,o).

TEM, HRTEM, SAED and AEM

TEM-HRTEM, SAED and qualitative AEM investigations were carried out on five samples (Table 1): 902R and 911R-g (Group I), and P9, P18 and 1002R (Group II).

Group I

Sample 902R shows the ubiquitous occurrence of volborthite, commonly occurring as polycrystalline angular to rounded grains between 3000 and 6000 Å in size, with clusters of platy anhedral to subhedral crystals stacked over each other (Figs. 6a and S2a). Observed using HRTEM, the lattice fringes of this mineral are clearly visible, and a SAED pattern shows a poorly crystalline behavior (Fig. 6a). The chemical composition of volborthite shows minor amounts of Zn (Figs. 6a and S2a), confirming observations from the EDS-WDS analysis (Table S2), with areas of elevated Mn content seeming to be associated with elevated Si (Figs. 6a and S2a; see also Fig. 3c-f).

This is the peer-reviewed, final accepted version for American Mineralogist, published by the Mineralogical Society of America.
The published version is subject to change. Cite as Authors (Year) Title. American Mineralogist, in press.
DOI: https://doi.org/10.2138/am-2023-9126. http://www.minsocam.org/

In sample 911R-g, vanadinite, mottramite and chrysocolla were identified (Figs. 6b and S2b). Chrysocolla was found together with vanadinite or mottramite particles; it has small amounts of Mg, K, and Ca, and showed a low crystallinity pattern in SAED. Mottramite contains some substituted As and Zn (Fig. 6b, see also Table S3), while its Si, Al, and Cl contents are likely due to fine intergrowths with chrysocolla and/or atacamite. HRTEM of vanadinite displays *d*-spacing of 8.9 Å (100), and a SAED a ring pattern with well-defined bright spots indicating a crystalline structure (Fig. 6b); chemically, minor As was present correlating with EDS data (Table S4).

Group II

In sample P9, TEM investigations identified volborthite, atacamite, Fe-rich oxides, and mixed Mn-Si-bearing phases (Figs. 7a and S3). Volborthite grains are in the range ca. 2000-5000 Å in size, and HRTEM of a particle shows well-defined *d*-spacings of 3 Å, corresponding to (-112); SAED image bright spots pattern indicating the presence of a well-crystallized individual. Tiny polycrystalline aggregates composed of volborthite and atacamite are also evident in SAED images of Fig. 7a. Chemically, volborthite has minor concentrations of As and Mn (Figs. 7a and S3; Table S2). Fig. S3 shows the occurrence of volborthite with atacamite; a Mn-Si-Al-rich phase was detected associated to volborthite in some samples and what is likely an Fe(Mg,Mn) oxide, potentially with included Ti-oxides, was also observed with the volborthite-atacamite clusters (Fig. S3).

In sample P18 vanadinite is found in triangular grains with clearly defined edges (Fig. 7b), ranging from ca. 500 to 3000 Å in size. An HRTEM image of vanadinite shows lattice fringe related to 3.4 Å *d*-spacing (102), whereas SAED investigations show a single crystal pattern with distinct spots although some are smaller and others diffuse (Fig. 7b). Mottramite occurs in aggregates between 2000 and 8000 Å in size, or in clusters of elongated crystals between 350 and 900 Å in length (Fig. S4a). Concentrations of As and Mn have also been detected in mottramite (Fig. S4a, see also Table S3). Rare

volborthite was observed in this sample (Fig. 7b), that had not been reported in the previous SEM-EDS and XRPD analyses. In Fig. S4a, chrysocolla envelops mottramite aggregates. As already observed in other samples, a Mn-Si-Al-rich phase occurs in close association with the vanadates (Fig. 7b).

In sample 1002R, mottramite and atacamite aggregates occur (Figs. 7c and S4b) with variable size. Observed on HRTEM (Fig. 7c), atacamite displays a *d*-spacing of 5.4 Å (101), and a corresponding SAED pattern. From the EDS spectrum, atacamite displays small concentrations of Si, Al, Pb, and V (Fig. 7c). A mottramite aggregate of ca. 500-2000 Å (Figs. S4b) shows a *d*-spacing of 2.6 Å (212), and the related SAED pattern with 4.0 Å (102) (Fig. S4b), with a chemical composition showing traces of Cl, Si and Al (Figs. 7c and S4b, Table S3).

FTIR spectroscopy

The IR spectra of the *vesbine*-bearing associations are complex, due to the heterogeneous nature of the samples which are mixtures of several mineral species. However, common features can be used to group the spectra: four types in the 400 cm^{-1} to 1800 cm^{-1} range, and five types in the 2000 cm^{-1} to 4000 cm^{-1} range (Table 3). The analysis of the spectra and the attribution of the different mineralogical phases present in the samples, was done considering the most prominent and sufficiently resolved absorptions (Table 4).

400 – 1800 cm^{-1} Region

Type I spectra (Fig. 8a) show a weak absorption at 1624 cm^{-1} due to the absorption of the H_2O ν_2 bending mode (Beran and Libowitzky, 2004). All the spectra are characterized by two strong doublets at around 1522 and 1498 cm^{-1} and 1419 and 1400 cm^{-1} which can be attributed to the absorptions of the ν_3 anti-symmetric stretching mode of the $[CO_3]^{2-}$ groups. The band at 1097 cm^{-1} is due to the ν_1

symmetric stretching mode of CO_3^{2-} group. Considering the mineralogical composition of these samples, it is reasonable to assign these absorptions to malachite and/or azurite. Bands present at 1049 cm^{-1} and at 883 cm^{-1} can be attributed to the bending vibrations of the Cu-OH^- bond in the structure of these minerals. Finally, the bands at 820 cm^{-1} and 752 cm^{-1} can be attributed to the ν_2 out-of-plane bending and ν_4 in-plane bending mode of $[CO_3]^{2-}$ group respectively. The bands at 987, 955 and 584 cm^{-1} can be assigned to the absorptions of atacamite. It should be noted that all these bands can be observed in all Type I samples but they are only well resolved in sample 997R. This is consistent with the occurrence of malachite (and minor azurite) in these samples except for sample $P18_{yellow}$. However, considering the high IR spectroscopy sensitivity, it is not possible to exclude the presence of small amounts of Cu-carbonates in $P18_{yellow}$ (see Table 4 for band assignments and references).

Type II (Fig. 8b) spectra show a weak and broad band at 1624 cm^{-1} due to the absorption of the H_2O ν_2 bending mode. From 1200 cm^{-1} to 600 cm^{-1} there is a strong multi-component absorption that can be partially resolved. Considering the mineralogical composition of the Type II samples, it is reasonable to assign these absorptions to volborthite and atacamite. In detail, the bands at 1093 cm^{-1} and 1047 cm^{-1} could be assigned to the Cu–OH^- bending vibrations of volborthite and atacamite respectively. The bands at 1012 cm^{-1} and 897 cm^{-1} can be assigned to the VO_3 symmetric terminal stretching of volborthite but the latter can be assigned also to the hydroxyl deformation in atacamite. The bands at 841, 781 cm^{-1} can be assigned to the VO_3 anti-symmetric stretching mode or/and to the V-O-V anti-symmetric bridge stretching. The bands at 766, 604, 577, 519 and 434 cm^{-1} can be tentatively assigned to atacamite and/or botallackite (Table 4).

Type III (Fig. 8c) spectra show the H_2O ν_2 absorption at 1624 cm^{-1} and a weak and broad absorption at around 1440 cm^{-1}. At about 1026 cm^{-1} there is a broad band with an accentuated tail on the low wavenumbers side with a weak shoulder at 1092 cm^{-1}. 911R-g, $P18G_{yellow}$ and 998R spectra show bands at 856, 787, 742, 605 and 520 cm^{-1}. The band at 1440 and 1026 cm^{-1} are assigned

501 respectively to chrysocolla and volborthite. The band at 1092 cm^{-1} is assigned to atacamite and/or
502 volborthite. The other bands are complex and can be variously interpreted as bands from the reference
503 spectra of descloizite, volborthite, mottramite and vanadinite. The $P9_{green}$ spectrum has some other
504 well-resolved components at 820, 706, 528, 505, 453 and 428 cm^{-1} all of which correlate to reference
505 spectra of botallackite (Table 4), which was identified in this sample by XRPD.

506 Type IV spectra (Fig. 8d) have the H_2O ν_2 absorption at 1624 cm^{-1} and a weak and broad
507 absorption at around 1440 cm^{-1}. These spectra are characterized by the occurrence of only one strong
508 absorption at around 1000 cm^{-1}, which is composed of several components more or less resolved.
509 Below 800 cm^{-1} there are many other weak absorptions. 911R-a spectrum has a quite pronounced
510 shoulder around 1124 cm^{-1} that can be assigned to the absorptions of the ν_3 antisymmetric stretching
511 vibration modes of the SO_4^{2-} tetrahedra (attributable to gypsum; see Table 2). In addition, the small
512 bands at 669 and 602 cm^{-1} could be assigned to the SO_4^{2-} ν_4 asymmetric bending vibration. Finally, all
513 the other components could be assigned essentially to atacamite and volborthite (Table 4).
514
515 ***3000 – 4000 cm^{-1} Region***
516 The spectra in this region are less complicated than those in the low frequency region, but this
517 makes the interpretation of these spectra even more complex than the spectra in the 400 – 1800 cm^{-1}
518 region.
519 Type A and type B spectra (Fig. 8e,f) are quite similar and can be assigned to atacamite and
520 malachite (Table 5). Type C spectra (Fig. 8g) can be resolved into four components that can be
521 assigned to malachite/azurite and atacamite (Table 5). Type D spectra have a single broad and weak
522 band centered at around 3465 cm^{-1} (Fig. S5).
523 It is not possible to group the remaining spectra of samples 997R, $P9_{green}$ and C5 in a single group
524 (Fig. 8h). 997R spectrum can be resolved into three components all of which can be assigned to

525 malachite (Table 5). $P9_{green}$ spectrum has four components that can be assigned to botallackite and
526 atacamite (Table 5). C5 spectrum has only one resolved component superimposed on a broad and
527 asymmetric absorption on the high wavenumbers side (Table 5), which is tentatively attributed to
528 azurite.
529
530
531 # DISCUSSION
532
533 ## Mineralogical characteristics of the main detected phases and comparison with previous
534 ## literature
535
536 ### *Vanadates*
537 Volborthite (15 samples), vanadinite (15 samples) and mottramite (13 samples) are the main
538 vanadates identified in the *vesbine* samples.
539 Volborthite composition ranges from almost stoichiometric to Mn-bearing varieties (in both
540 Group I and Group II samples). Its mean chemical formula (calculated from 14 selected analyses, Table
541 S2) can be expressed as:
542 $$(Cu_{2.94}Zn_{0.02}Pb_{0.02}Mn_{0.15})_{\Sigma=3.13}(V_{2.06}P_{0.01})_{\Sigma=2.07}O_7(OH)_{2.01}\cdot 2.04H_2O.$$
543 Other minor elements (Si, Al, Ca, K, Ba, Fe, Mg and S) could derive from contamination from
544 silicates of the host rock.
545 Impurities of Si, S, Al, Cl, Ca, and Fe were found in volborthite (with atacamite) in fractures and
546 on the surfaces of lava blocks on the northeast slope of the Alaid volcano (Atlasov island, Kuril
547 Islands, Russia, Zhitova et al., 2021). Fine intergrows of volborthite-silicate-Mn-Ba oxide (potentially
548 hollandite or romanéchite) can be suggested by significant Mn amounts (with minor Ba-Si-Al), locally

549 detected by TEM and EDS analyses in sample 902R. However, clear evidence for the presence and
550 speciation of specific Mn-bearing oxides (present in two samples from the Mineralogical Museum's
551 catalog, see Table 1), requires further investigation, particularly because hausmannite has been reported
552 in the literature in the vesbine samples (Russo and Punzo, 2004). A further speculation, particularly for
553 two samples (P9 and 902R), is the possibility that the mixed phase V-Cu Mn-Si-Al-(+Ba) might be a
554 precursor of vésigniéite.

555 Like volborthite, mottramite analyses showed a composition varying from nearly stochiometric to
556 containing minor amounts of various elements. Mottramite has the following average empirical
557 formula: (from 12 selected analyses, Table S3):

558 $$(Cu_{0.98}Zn_{0.01}Mn_{0.02}Fe_{0.01})_{\Sigma=1.02}Pb_{1.00}(V_{0.90}As_{0.05})_{\Sigma=0.95}O_4(OH)_{1.00}.$$

559 Russo and Punzo (2004) reported a qualitative EDS spectrum of yellow spherules in a *vesbine*
560 sample from Vesuvius (*Villa Inglese*), with significant amounts of Si, Al, K, Ca, Mn, Ba and As, which
561 probably corresponds to a mottramite (mixed with a silicate) or a lead-bearing volborthite. Secondary
562 (supergene) mottramite and volborthite-rich associations are described by Shchipalkina et al. (2020,
563 and references therein) in some paleofumarolic fields of the Tolbachik volcano.

564 Descloizite was suggested from XRPD and FTIR in both Group I and Group II samples.
565 However, considering it forms a series with mottramite, chemical confirmation is desirable, since
566 throughout this study there was no clear chemical determination of descloizite.

567 Vanadinite is a widespread phase in Group I and particularly in Group II samples. Its average
568 chemical formula (from ten selected analyses, Table S4) is:

569 $$(Pb_{9.08}Cu_{0.98}Mn_{0.02}Fe_{0.01})_{\Sigma=10.09}(V_{5.00}As_{0.18}P_{0.19})_{\Sigma=5.37}O_{24}Cl_{2.06.}$$

570 Solid solution with pyromorphite and/or mimetite (Antao and Dhaliwa, 2018) is also detected in
571 one sample. Small amounts of Mn, Cu, and As were detected in vanadinite from RMMN *vesbine*

572 samples by Balassone et al. (2019). Furthermore, a vanadinite occurrence related to fumarolic minerals
573 formed after the 1944 AD eruption of Vesuvius, was documented by Russo (2018).

574 A supposed starovaite, a rare anhydrous K-Cu-bearing vanadate first found in fumarole
575 sublimates of the Tolbachik volcano (Pekov et al., 2013), could be present in one sample (911R-b,
576 Group I), also showing minor contents Pb, Mn, and As, but it was not observed in the XRPD pattern.
577 Balassone et al. (2019) detected starovaite with minor Zn and Mn in one of the RMMN vesbine
578 samples with atacamite, while starovaite from the type-locality contains minor Zn, Pb, As and Mo
579 occur (Pekov et al., 2013). Further investigation is needed to determine the identity of this Cu-K
580 vanadate found in the investigated sample.
581
582 ***Cu-hydroxychlorides***
583 Atacamite is common amongst samples studied and is a main component of the thin green crusts
584 forming the Vesuvian sublimates (Coradossi et al., 1980; Russo and Punzo, 2004). Its composition can
585 be expressed by the average empirical formula $(Cu_{1.95}Mn_{0.01}Mg_{0.01}Pb_{0.01})_{\Sigma=1.98}Cl_{1.06}OH_{2.90}$ (from
586 selected fifteen analyses, Table S5). TEM investigations of sample 911R-g, characterized by its higher
587 Mn amounts (3.3-5.2 wt.% MnO), did not produced reliable data, so it is not possible to determine if
588 Mn is admixed from a different mineral species or is a direct substitution of Cu for Mn. The other two
589 polymorphs of $Cu_2(OH)_3Cl$, clinoatacamite and botallackite, were detected both by XRPD and FTIR
590 analyses. The presence of sub-millimetric crystals of clinoatacamite was already reported by Russo and
591 Campostrini (2021) in a *vesbine* sample from the Vesuvian site of *Villa Inglese*, whereas the occurrence
592 of botallackite, a polymorph of $Cu_2(OH)_3Cl$ reported in this study, is the first time that it is recorded at
593 Vesuvius. Botallackite, the rarest of the naturally occurring copper hydroxy-chlorides (Hawthorne,
594 1985; Krivovichev et al., 2017), recrystallizes quickly under most conditions to more stable

595 polymorphs and thus might only be preserved if the solutions responsible for its crystallization are
596 quickly removed from the system (Pollard et al., 1989).

597 Paratacamite was detected by XRPD, however significant concentrations of Zn, which could
598 corroborate its identification, were not observed in any of the chemical analyses. This mineral was
599 previously identified at Vesuvius (Balassone et al., 2019; Russo, 2021, and references therein).

600

601 ***Other minerals***

602 Concerning malachite and azurite, carbonates are uncommon at Vesuvius and fumarolic
603 environments in general, due to the typically highly acidic conditions that make most carbonates
604 unstable (Balić-Žunić et al., 2016).

605 Also, Cu-bearing silicates (here represented by chrysocolla and potentially dioptase) are
606 uncommon at Vesuvius; chrysocolla is observed only in a few samples from recent activity (Russo and
607 Punzo, 2004; Russo and Campostrini, 2011; Balassone et al., 2019; Russo, 2021).

608 Wulfenite was documented for the first time by Balassone et al. (2019) in one RMMN sample
609 with a mottramite-vanadinite-chrysocolla assemblage. Across the whole Somma-Vesuvius complex,
610 wulfenite was only recorded by Russo et al. (2009) in the San Vito metamorphosed ejecta. Africano et
611 al. (2002) documented wulfenite precipitated from high-temperature volcanic fumarole gases in the
612 Satsuma-Iwojima volcano (Japan). As regards stolzite, this is the first recorded occurrence at Somma-
613 Vesuvius complex. The variable amount of W found by Zambonini and Carobbi (1927) in the vesbine
614 samples, at that time not ascribed to a separate mineral, could have been due to stolzite.

615 The copper oxides cuprite and tenorite are uncommon phases in the studied mineral assemblage.
616 At Vesuvius, and generally in fumarolic environments, cuprite is rare: it has been detected in Vesuvius
617 lavas (see Russo and Punzo, 2004) in association with atacamite, as well as in a sample containing
618 atacamite, volborthite and fluorite (Balassone et al., 2019). Tenorite is more widespread and has been

identified in various rocks related to the lavas from Medieval times to 1944 AD lavas (Russo and Punzo, 2004). As reported by Russo and Punzo (2004), tenorite is typical of the high-T fumaroles and can be subsequently altered to paratacamite.

Undetermined Mn (± Zn,Ba)-rich phases, as well as traces of Fe-oxy-hydroxides are observed in some samples from both groups.

The formation environment and paragenesis

In the *vesbine* samples studied, Cu-bearing minerals dominate, with the Cu-V phases being the most common.

In volcanic exhalations Cu-V minerals are rare, but it is worth noting that all known natural anhydrous copper vanadates come from fumarolic environments (Zhitova et al., 2021, and references therein).

Volborthite and mottramite are recognized as relatively common minerals in the supergene environment, formed from the weathering of exhumed Cu-Zn-sulfide deposits (e.g., Sillitoe, 2005). However, volborthite has been recently described in the volcanically related environments of the Alaid volcano (Kuril Islands) and in paleofumaroles of the Mountain 1004 (Tolbachik, Kamchatka), both located in Russia (Zhitova et al., 2021; Ismagilova et al., 2021). For these occurrences, the proposed formation is via the alteration of primary fumarolic Cu and V minerals. Ismagilova et al. (2021) suggested many potential fumarolic minerals that could serve as a source of Cu and V. Zhitova et al. (2021) surmised that euchlorine [$KNaCu_3O(SO_4)_3$] and shcherbinaite (V_2O_5) could be the Cu and V sources for volborthite, respectively; they also suggested a scheme for the formation of an association of volborthite and atacamite by replacing the anhydrous copper vanadate stoiberite $Cu_5(VO_4)_2O_2$:

$$Cu_5(VO_4)_2O_2 + HCl + 4H_2O = Cu_3V_2O_7(OH)_2 \cdot 2H_2O + Cu_2Cl(OH)_3.$$

643 This reaction allows for the formation of atacamite at low temperature (100-150°C).

644 Vanadinite is also almost always found as a secondary mineral in the oxidation zone of lead
645 deposits, resulting from the alteration of vanadium-bearing sulfides and silicates (Anthony et al., 2000;
646 Boni et al., 2009).

647 Atacamite is found in fumarolic deposits, in exhalative red-bed copper mineralization (Sillitoe
648 and Rodriguez, 2022), and is also a common secondary copper mineral deriving from oxidation of
649 primary Cu ores, especially under arid and saline conditions (Anthony et al., 2000, Chavez, 2000;
650 Sillitoe, 2005; Reich et al., 2008).

651 Malachite, azurite and chrysocolla are commonly found as secondary minerals in weathered
652 portions of many copper sulfide deposits (Anthony et al., 2000), whereas they are poorly represented in
653 volcanic exhalation products.

654 Pekov et al. (2018) reported that fumaroles containing copper mineralization occur in a few
655 (mainly active) volcanoes (main occurrences: Tolbachik, Russia; Vesuvius, Italy; Izalco, El Salvador;
656 Eifel, Germany), with the fumarolic copper minerals crystallizing over a wide temperature interval,
657 from 650–750 °C down to 50–70 °C. The unique combination of high temperature, atmospheric
658 pressure, and gaseous transport of most constituents causes the distinctive nature of fumarolic
659 mineralization. According to Pekov et al. (2018), copper minerals of the fumarolic systems can be
660 subdivided into two genetic groups depending on their temperature of crystallization: minerals formed
661 in the hot zones of fumaroles (>200°C, mainly in the range 300-700 °C, defined by these authors as
662 Group I), and minerals formed in the moderately hot zones of fumaroles (<200 °C, mainly at 100-150
663 °C, defined as Group II). Representatives of these groups are quite different in terms of their chemistry
664 and crystal chemistry. The high-temperature fumarolic minerals include only H-free minerals. Hence,
665 Pekov et al. (2018) stated that the absence of hydrogen is their most defining chemical feature. For
666 instance, these authors considered a few anhydrous minerals to belong to this type, such as vanadates

667 (blossite, fingerite, leningradite, mcbirneyite, kainotropite, etc., along with starovaite; Pekov et al.,
668 2013, 2020a,b) and oxides (tenorite). Moreover, at the Tolbachik exhalations (Russia) Pekov et al.
669 (2023) recently discovered bakakinite, $Ca_2V_2O_7$, another H-free vanadate formed at a temperature not
670 lower than 500ºC. For the anhydrous copper vanadates discovered at the Izalco fumaroles (El
671 Salvador), Hughes and Stoiber (1985) reported very high T, in the 690-760 °C range.

672 Pb-tungstates and molybdates occur in the *vesbine* paragenesis investigated here. Wulfenite is
673 commonly a secondary mineral found in the oxidized zones of hydrothermal lead deposits, whereas
674 stolzite is a rare secondary mineral in the oxidized zones mainly of hydrothermal tungsten-bearing lead
675 deposits (Antony et al., 2002). Africano et al. (2002) reported the first occurrence of wulfenite at the
676 Satsuma-Iwojima volcano (Japan), formed by precipitation between 540 and 490 °C from a gas with
677 lower sulfur content and/or higher fO_2 and a higher Mo content than the Satsuma-Iwojima gases
678 reported in the previous literature.

679 Subordinate amounts of tenorite have been observed in the studied samples. This mineral is
680 typical of the high temperature Vesuvian fumaroles (K–Na salts bearing, T >400 °C, Balić-Žunić et al.
681 2016, and references therein) and originates from interaction of gaseous $CuCl_2$ and water vapor,
682 according to the reaction: $CuCl_2 + H_2O = CuO + 2HCl$ (Russo and Punzo, 2003; Angus and Davis,
683 1976). Tenorite can be subsequently altered by HCl brines to form paratacamite (Russo and Punzo,
684 2004; Balić-Žunić et al., 2016).

685 Angus and Davis (1976) discussed the transport mechanism of Cu, Pb, Zn and other alkali metals
686 in volcanic sublimates and secondary alteration products from Vesuvius and Vulcano, with an interest
687 in its relevance to economic geology. Based on previous literature reporting the distillation of cuprous
688 chloride gas from lava and its direct sublimation to form atacamite, they suggested that these metals
689 were transported as volatile chlorides. The same authors also hypothesized that volatilization as a
690 chloride was not the only way in which metals were transported in volcanic gases, suggesting the

transport of elements such as vanadium, molybdenum, manganese, and iron as volatile carbonyl compounds.

An apparent paragenetic sequence of the Vesuvian *vesbine*, based on the observations of the new sample set is presented in Fig. 9, and some important genetic aspects can be highlighted:

1. the copper oxides are the first phases to crystallize;
2. wulfenite and stolzite can be present in at least two generations, which can also pre-date the volborthite and mottramite crystallization;
3. volborthite and mottramite appear to crystallize in different generations, and vanadinite generally pre-dates them;
4. the Cu-hydroxychlorides can be deposited in multiple generations, as late phases after volborthite and mottramite or also co-genetic with volborthite;
5. the Cu-bearing carbonates and silicates are deposited after the vanadates;
6. gypsum and cerussite are the last phases in the paragenetic sequence, along with rare sylvite, they likely formed as late-stage alteration minerals.

The mineralogical evidence from this study and the literature data suggests an approximate temperature range between ca. 100 °C and 400 °C for the formation of *vesbine*, with the OH/H_2O free minerals likely formed at higher temperatures, followed by the hydrated phases deposited in lower T conditions. A higher upper temperature may be suggested by the wulfenite-stolzite, tenorite and cuprite occurrences, however, the occurrence of hydrous vanadates together with anhydrous phases (vanadinite, and possibly the rare starovaite) may indicate lower temperatures compared to other worldwide occurrences, where only anhydrous vanadates have been found (see Hughes and Stoiber, 1985; Pekov et al., 2018).

However, the temperature regime, as well as the chemical composition of the fluids, can change even over relatively short periods of time during the fumarolic activity. This can lead to cyclic

This is the peer-reviewed, final accepted version for American Mineralogist, published by the Mineralogical Society of America.
The published version is subject to change. Cite as Authors (Year) Title. American Mineralogist, in press.
DOI: https://doi.org/10.2138/am-2023-9126. http://www.minsocam.org/

crystallization of hydrated minerals at lower temperatures, and potentially dehydration for some minerals when temperatures increase (Siidra et al., 2021).

According to Balić-Žunić et al. (2016), the mixing of several mineral associations is a frequent phenomenon in fumarolic environments. Hence, the complexity of the mineral assemblages observed in this study could be ascribed to the oscillation of both temperature and chemical compositions in very restricted spaces. For the samples studied, post depositional alteration phenomena, i.e., hydration from being open to the atmosphere and stored in collections and/or out in the field for decades, can also be considered.

The origin of vanadium-rich sublimates

To explain the origin of the vanadate-bearing association found in the Izalco volcano, Hughes and Stoiber (1985) discussed the conditions required for the vanadium-bearing gases to form high-T and V-rich sublimation deposits. They determined a minimum temperature of 760°C for ziesite ($Cu_2V^{5+}{}_2O_7$), based on geothermometry calculated from phase relations in the system $CuO\text{-}V_2O_5$, while the formation temperature of shcherbinaite (V_2O_5) and bannermanite [$(Na,K)_xV^{4+}{}_xV^{5+}{}_{6-x}O_{15}$], was ~690°C. In consideration of these high temperatures, which existed at the time of sublimation of the vanadium compounds and noting that the reaction of wall rock with acid gases is significant only at lower temperatures (<300°C), a magmatic source for vanadium was suggested. Among the various vanadium compounds existing in a gaseous state at magmatic temperatures, the only gases that contain V^{3+} (the stable oxidation state at that T and f_{O2}, as calculated from $V_2O_3\text{-}V_2O_4$ equilibria) are VF_3 and VOCl, suggesting that one or both these gases could be responsible for the segregation of vanadium from the magma. These authors, observing that Izalco is dominated by the system V-O-Cl gases,

738 suggested that vanadium oxychloride gases sublimed through the reaction (with first VOCl oxidized to
739 $VOCl_3$ while rising to the surface):

740 $$2VOCl_{3(v)} + 3H_2O_{(v)} \rightarrow V_2O_{5(s)} + 6HCl_{(v)}$$

741 Hughes and Stoiber (1985) thus suggested that V-bearing gases could be exsolved from a magma
742 with "normal" basaltic concentrations of V (average V concentration of Izalco basaltic rocks equal to
743 266 ppm), to produce vanadium compounds in response to the changing conditions of temperature, f_{O2},
744 and/or pH.

745 Chemical data regarding specific trace elements, on Somma-Vesuvius lava flows of medieval age
746 or older, can be extrapolated from literature. For instance, Di Renzo et al. (2007) documented the
747 following average values for various products: V 131 ppm, Cu 25 ppm, Zn 140 pp, Pb 34 ppm, W 3.9
748 ppm (from 18.3 to 16 ka deposits); V 232 ppm, Cu 95 ppm, Zn 86 pp, Pb 37 ppm, W 6.4 ppm (from
749 3.7 ka to 79 AD deposits). Avanzinelli et al. (2008) analyzed five samples from Vesuvius, with ages
750 spanning from 1.26 to 1.00 ka, resulting in the following values for V and Cu (Pb, W and Zn were not
751 analyzed for these samples): V 268-228 ppm, Cu 68-112 ppm (lapilli fall, 1.26 ka); V 242 ppm, Cu 119
752 ppm (lapilli fall, 1.00 ka). For recent lavas, the authors also reported the following data: V 194 ppm, Cu
753 99 ppm (lava, 1858 AD); V 230 ppm, Cu 101 ppm (lava, 1944 AD).

754 Joron et al. (1987) reported Fe-Ti oxide in lava likely ascribed to the 986-1037 AD eruptive event
755 of Vesuvius, which showed a V_2O_3 content of 0.75 wt.% (corresponding to ca. 5100 ppm V). These
756 authors also reported the vertical change of V amounts in eruptive fall sequences of Plinian and sub-
757 Plinian events (15.5 ka –79 AD), having a range in values of ca. 10-100 ppm (Mottana, 1998).

758 MacDonald et al. (2016) reported many analyses of clinopyroxenes from lava and *scoriae*
759 samples taken at the *Cercola* eccentric cone and on the *Pollena* parasitic cones, exposed in the *Pollena*
760 quarry (the age of these two groups of volcanic structures being certainly older than 20,000 years, and

761 overlapping the period of construction of the Somma stratovolcano, 39–25 ka). The maximum amount
762 of V in clinopyroxene phenocrysts is 0.17 wt.% V_2O_3 (ca. 1200 ppm).

763 It is also worth mentioning that vanadium amounts found in medieval lava are of the same order
764 of magnitude as those in the Izalco basalts. An epigenetic selective mechanism of uptake from host
765 rocks by circulating fluids may explain the enrichment (remobilization) of V (and base metals) in the
766 encrustations deposited on lava surfaces and in fractures for these occurrences.
767
768
769 ## IMPLICATIONS
770
771 This study has helped to further define the complex mineralogy of *vesbine*, a product of the
772 fumarolic activity of Vesuvius volcano that is poorly understood. It has also enhanced the knowledge
773 of the complex geochemistry and mineralogy of Vesuvius more generally. Hence, the analysis of these
774 associations of fumarolic origin, since they are directly connected and controlled by the chemistry and
775 the temperature of the volcanic gases, can be useful indicators both in the reconstruction of the activity
776 of extinct volcanoes and, above all, in the monitoring of still active volcanoes.

777 Among the main components vanadates are prevailing, with widespread vanadinite, mottramite
778 and volborthite, making this association an example of a vanadium-rich sublimate deposit. The possible
779 occurrence of starovaite may be an important genetic clue because, according to literature, this type of
780 OH/H_2O-free mineral in the exhalative environment is commonly related to high temperature
781 conditions. Several minor and trace elements such as Mn, Zn, and As are detected in the vanadates in
782 significant amounts. Contrary to Zambonini and Carobbi (1927), no significant La, Ce, Nd, Dy, Y, Ta,
783 Nb or Co have been detected in the *vesbine* associations, even when investigated at the nanoscale with
784 the HRTEM. The occurrence of wulfenite and stolzite-rich phases testify a Mo and W enrichment in

the fluid, along with Pb. It is worth noting that, to the authors' knowledge, wulfenite was only recorded in some Somma-Vesuvius metamorphosed ejecta, but never in the fumarolic mineral associations, whereas stolzite has never been recorded in this volcanic complex up to now.

The genetic implication is that these exhalative products are related to fumaroles, which had oxidizing conditions: these are less common than those with reducing environments (Siidra et al., 2021). They can be formed by a combination of different processes:

1. rock-fluids interaction, leaching and remobilization of wall rock components by metals-bearing solutions;
2. gas-water interaction, represented by the reaction between groundwater and ascending fluids;
3. alteration/oxidation of primary fumarolic minerals.

In general, OH/H_2O-free minerals and copper oxides (wulfenite/stolzite, tenorite, cuprite) should be related to higher T conditions, while other phases are clearly related to lower temperatures (for instance, gypsum may have been formed through the last phases of fumarolic activity). Different generations of minerals can be observed, also determined by the fluctuation of conditions on a small scale at the interface between volcanic gases and the atmosphere.

Finally, it is worth mentioning that nowadays the vanadium-bearing minerals are also of interest for economic geology and renewable energy technologies, since the use of vanadium, one of the so-called critical metals in both USA and in Europe (European Commission, 2023; U.S. Geological Survey, 2022, 2023), has risen substantially in recent years in innovation-driven industries that depend on this metal for their operations and products (U.S. Geological Survey, 2023). For this reason, any study dealing with the depositional features of this element could have interesting implications and could be useful for exploration.

ACKNOWLEDGEMENTS

This work is part of the ongoing PhD of Annamaria Pellino at the DiSTAR (University of Naples Federico II, Italy). The authors are grateful to the Associated Editor, Prof. Lindsay McHenry, for helpful advice and to T.L. Panikorovskii and an anonymous reviewer, whose insightful comments have significantly improved the quality of the paper. M. Boni is thanked for useful discussions. We are indebted to S. Bravi for careful preparation of thin sections and R. de Gennaro (DiSTAR) for technical help during SEM-EDS analyses. We thank M.M. Abad-Ortega and C. de la Prada Sánchez (CIC, Granada, Spain) for the skillful support during TEM analyses. TEM research was supported by the project PGC2018-094573-B-I00 from the MCIU-AEIFEDER and the research group RNM-325 of the Junta de Andalucía (Spain). Thanks are also due to Dr. Francesco Baldassarre (IC-CNR, Bari, Italy) for X-ray data collection. This research received support from the SYNTHESYS+ Project http://www.synthesys.info/ which is financed by European Community Research Infrastructure Action under the H2020 Integrating Activities Programme, Project number 823827 granted to N. Mondillo.

REFERENCES CITED

Africano, F., Van Rompaey, G., Bernard, A., Le Guern, F. (2002) Deposition of trace elements from high temperature gases of Satsuma- Iwojima volcano. Earth Planets Space, 54, 275–286.

Altomare, A., Corriero, N., Cuocci, C., Falcicchio, A., Moliterni, A., Rizzi, R. (2015) QUALX2.0: a qualitative phase analysis software using the freely available database POW_COD. Journal of Applied Crystallography, 48, 598-603.

Anbalagan, G., Mukundakumari, S., Murugesan, K.S., Gunasekaran, S. (2009) Infrared, optical absorption, and EPR spectroscopic studies on natural gypsum. Vibrational Spectroscopy, 50, 226–230.

Angus, J.G., Davis, G.R. (1976) Base metal enrichment in volcanic sublimates and secondary alteration products from Vesuvius and Vulcano. Mineralogical Magazine, 40, 481-486.

Antao, S.M., Dhaliwa, I. (2018) Lead apatites: structural variations among $Pb_5(BO_4)_3Cl$ with B = P (pyromorphite), As (mimetite) and V (vanadinite). Journal of Synchrotron Radiation, 25, 214–221.

Anthony, J.W., Bideaux, R.A., Bladh, K.W., Nichols, M.C. (2000) Handbook of Mineralogy, Volume IV. Arsenates, Phosphates, Vanadates. Mineral Data Publishing, Tucson, AZ, 680 pp.

Arvind, H.K., Kalal, S., Punjabi, P.B., Choudhary, B.L., Dolia, S.N., Kumar, S. (2016) Structural, optical and magnetic behaviour of nanocrystalline volborthite. AIP Conference Proceedings 1728, 020336.

Avanzinelli R., Elliott T., Tommasini S., Conticelli S. (2008) Constraints on the genesis of the potassium-rich Italian volcanics from U/Th disequilibrium. Journal of Petrology, 49, 195-223.

Balassone, G., Petti, C., Mondillo, N., Panikorovskii, T.L., de Gennaro, R., Cappelletti, P., Altomare, A., Corriero, N., Cangiano, M. and D'Orazio, L. (2019) Copper Minerals at Vesuvius Volcano (Southern Italy): a mineralogical review. Minerals, 9, 730.

Balić-Žunić, T., Garavelli, A., Jakobsson, S.P., Jonasson, K., Katerinopoulos, A., Kyriakopoulos, K., and Acquafredda, P. (2016) Fumarolic Minerals: An Overview of Active European Volcanoes. In K. Nemeth (Ed.), Updates in Volcanology - From Volcano Modelling to Volcano Geology, 267-322.

Bartholomäi, G., Klee, W.E. (1978) The vibrational spectra of pyromorphite, vanadinite and mimetite. Spectrochimica Acta, 34A, 831–843.

855 Bayat, A., Mahjouba, A.R., Amini, M.M. (2018) Facile hydrothermal synthesis of the colloidal
856 hierarchical Volborthite ($Cu_3V_2O_7(OH)_2 \cdot 2H_2O$) hollow sphere phosphors. Journal of
857 Luminescence, 204, 382–385.
858 Beran, A., Libowitzky, E. (eds) (2004) Spectroscopic methods in mineralogy. EMU Notes in
859 Mineralogy, vol 6, p 670.
860 Bishop, J.L., Lane, M.D., Dyar, M.D., King, S.J., Brown, A.J., Swayze, G.A. (2014) Spectral
861 properties of Ca-sulfates: Gypsum, bassanite, and anhydrite. American Mineralogist, 99, 2105–
862 2115.
863 Boni, M., Balassone, G., Arseneau, V., Schmidt, P. (2009) The nonsulfide zinc deposit at Accha
864 (Southern Peru): geological and mineralogical characterization. Economic Geology, 104, 267-
865 289.
866 Braithwaite, R.S.W., Mereiter, K., Paar, W.H., Clark A.M. (2004) Herbertsmithite, $Cu_3Zn(OH)_6Cl_2$, a
867 new species, and the definition of paratacamite. Mineralogical Magazine, 68, 527–539.
868 Brown, R.G., Ross, S.D. (1972) The vibrational spectra of some condensed tetrahedral anions $[X_2O_7]^{n-}$.
869 Spectrochimica Acta, 28A, 1263–1274.
870 Busca, G., Ricchiardi, G., Sam, D.S.H., Volta, J-C. (1994) Spectroscopic characterization of
871 magnesium vanadate catalysts Part 1. – Vibrational characterization of $Mg_3(VO_4)_2$, $Mg_2V_2O_7$,
872 and MgV_2O_6 powders. Journal of the Chemical Society, Faraday Transactions, 90, 1161–1170.
873 Caliro, S., Chiodini, G., Avino, R., Minopoli, C., Bocchino, B. (2011) Long time series of chemical
874 and isotopic compositions of Vesuvius fumaroles: evidence for deep and shallow processes.
875 Annals of Geophysics, 54, 137-149.
876 Chávez, W.X. (2000) Supergene Oxidation of copper deposits: zoning and distribution of copper oxide
877 Minerals. SEG Discovery, 41, 1–21.

878 Chiodini, G., Marini, L., Russo, M. (2001) Geochemical evidence for the existence of high-temperature
879 hydrothermal brines at Vesuvio volcano, Italy. Geochimica and Cosmochimica Acta, 65, 2129-
880 2147.
881 Chukanov, N.V. (2014) Infrared spectra of mineral species: Extended library. Springer
882 Geochemistry/Mineralogy .
883 Chukhrov, F.V., Zvyagin, B.B., Gorshkov, A.I., Yermilova, L.P., Rudnitskaya, Ye.S. (1969)
884 Chrysocollas. International Geology Review, 11.
885 Cioni, R., Santacroce, R., Sbrana, A. (1999) Pyroclastic deposits as a guide for reconstructing the
886 multi-stage evolution of the Somma-Vesuvius Caldera. Bulletin of Volcanology, 61, 207-222.
887 Cioni, R., Bertagnini, A., Santacroce, R., Andronico, D. (2008) Explosive activity and eruption
888 scenarios at Somma-Vesuvius (Italy): towards a new classification scheme. Journal of
889 Volcanology and Geothermal Research, 178, 331–346.
890 Cioni, R., D'Oriano, C., Bertagnini, A., Andronico, D. (2013) The 2nd to 4th century explosive activity
891 of Vesuvius: new data on the timing of the upward migration of the post-A.D. 79 magma
892 chamber. Annals of Geophysics, 56, 4, 2013, S0438.
893 Conticelli, S., Laurenzi, M.A., Giordano, G., Mattei, M., Avanzinelli, R., Melluso, L., Tommasini, S.,
894 Boari, E., Cifelli, F., Perini, G. (2011) Leucite-bearing (kamafugitic/ leucititic) and –free
895 (lamproitic) ultrapotassic volcanic rocks and associated shoshonites in the Italian Peninsula:
896 constraints on petrogenesis and geodynamics. In: Beltrando, M., Peccerillo, A., Mattei, M.,
897 Conticelli, S., Doglioni, C. (Eds.), The Geology of Italy, Journal of Virtual Exploration, 36, paper
898 20, 94 p.
899 Coradossi, N. (1980) I sublimati. Rendiconti della Società di Mineralogia e Petrologia, 36, 573-584.

Del Pezzo, E., Chiodini, G., Caliro, S., Bianco, F., Avino, R. (2013) New insights into Mt. Vesuvius hydrothermal system and its dynamic based on a critical review of seismic tomography and geochemical features. Annals of Geophysics, 56, 4, S0444.

De Luise, L. (1914) Secondo contributo alla "Notizia della eruzione vesuviana del 1906". Stab. Tip. E. della Torre, Portici (NA), p. 17.

Deville Saint-Claire, C. (1855) Observations sur la nature et la distribution des fumerolles dans l'eruption du Vesuve du 1855. Mallet-Bachier imprimeur-libraire, 55, Paris.

De Waal, D., Hutter, C. (1994) Vibrational spectra of two phases of copper pyrovanadate and some solid solutions of copper and magnesium pyrovanadate. Materials Research Bulletin, 29, 843–849.

Di Renzo, V., Di Vito, M.A., Arienzo, I., Carandente, A., Civetta, L., D'Antonio, M., Giordano, F., Orsi, G., Tonarini, S. (2007) Magmatic History of Somma Vesuvius on the basis of New Geochemical and Isotopic Data from a Deep Borehole (Camaldoli della Torre). Journal of Petrology, 48, 753-784.

European Commission (2023) Study on the Critical Raw Materials for the EU 2023 - Final Report. 158 p.

Frondini, F., Chiodini, G., Caliro, S., Cardellini, C., Granieri, D., Ventura, G. (2004) Diffuse CO_2 degassing at Vesuvio, Italy. Bulletin of Volcanology, 66, 642-651.

Hawthorne, F.C. (1985) Refinement of the crystal structure of botallackite. Mineralogical Magazine, 49, 87-89.

Frost, R.L., Xi, Y. (2013) Is chrysocolla $(Cu,Al)_2H_2Si_2O_5(OH)_4 \cdot nH_2O$ related to spertiniite $Cu(OH)_2$?—A vibrational spectroscopic study. Vibrational Spectroscopy, 64, 33–38.

Frost, R.L., Crane, M., Williams, P.A., Kloprogge, J.T. (2003) Isomorphic substitution in vanadinite $[Pb_5(VO_4)_3Cl]$ – a Raman spectroscopic study. Journal of Raman Spectroscopy, 34, 214–220.

924 Frost, R.L., Palmer, S.J., Čejka, J., Sejkora, J., Plášil, J., Bahfenne, S., Keeffe, E.C. (2011) A Raman
925 spectroscopic study of the different vanadate groups in solid-state compounds – model case:
926 mineral phases vésignéite [$BaCu_3(VO_4)_2(OH)_2$] and volborthite [$Cu_3V_2O_7(OH)_2 \cdot 2H_2O$]. Journal
927 of Raman Spectroscopy, 42, 1701–1710.
928 Frost, R.L., Martens, W., Kloprogge, J.T. Williams, P.A. (2002a) Raman spectroscopy of the basic
929 copper chloride minerals atacamite and paratacamite: implications for the study of copper, brass
930 and bronze objects of archaeological significance. Journal of Raman Spectroscopy, 33, 801–806.
931 Frost, R.L., Martens, W.N.,Rintoul, L., Mahmutagic, E., Kloprogge, J.T. (2002b) Raman spectroscopic
932 study of azurite and malachite at 298 and 77 K. Journal of Raman Spectroscopy, 33, 252–259.
933 Frost, R.L., Williams, P.A., Kloprogge, J.T., Leverett, P. (2001) Raman spectroscopy of descloizite and
934 mottramite at 298 and 77 K. Journal of Raman Spectroscopy, 32, 906-911.
935 Frost, R.L., Xi, Y., López, A., Corrêa, L., Scholz, R. (2014) The molecular structure of the vanadate
936 mineral mottramite $PbCu(VO_4)(OH)$] from Tsumeb, Namibia – A vibrational spectroscopic
937 study. Spectrochimica Acta Part A: Molecular and Biomolecular Spectroscopy, 122, 252–256.
938 Gao, J., Yuan, X. (2020) Vibrational investigation of pressure-induced phase transitions of
939 hydroxycarbonate malachite $Cu_2(CO_3)(OH)_2$. Minerals, 10, 277.
940 Goldsmith, J.A., Ross, S.D. (1968) The infra-red spectra of azurite and malachite. Spectrochimica
941 Acta, 24, 2131-2137.
942 Hass, M., Sutherland, G.B.B.M. (1956) The infra-red spectrum and crystal structure of gypsum.
943 Proceeding The Royal Society of London A, 236, 427–445.
944 Hughes, J.M., Stoiber, R.,E., (1985) Vanadium sublimates from the fumaroles of Izalco Volcano, El
945 Salvador. Journal of Volcanology and Geothermal Research, 24, 283-291.
946 ICDD (2003) The Powder Diffraction File. International Center for Diffraction Data, 12 Campus
947 Boulevard, Newton Square, Pennsylvania 19073-3273, USA.

948 Ismagilova, R.M., Zhitova, E.S., Krivovichev, S.V., Sergeeva, A.V., Nuzhadaev, A.A., Anikin, L.P.,
949 Krzhizhanovskaya, M.G., Nazarova, M.A., Kupchinenko, A.N., Zolotarev, A.A., Kutyrev, A.V.,
950 Bukhanova, D.S., Kuznetsov, R.A., Khanin, D.A. (2021) Phase evolution from volborthite,
951 $Cu_3(V_2O_7)(OH)_2.2H_2O$, upon heat treatment. Minerals, 11-1312, 1-14.
952 Joron, J.L., Metrich, N., Rosi. M., Santacroce R. (1987) Chemistry and petrography. In (Santacroce R.,
953 Ed.): Somma-Vesuvius, Quaderni del "La ricerca scientifica", 114, vol. 8, 251 p., 105-174.
954 Krivovichev, S.V., Hawthorne, F.C., Williams, P.A. (2017): Structural complexity and crystallization:
955 the Ostwald sequence of phases in the $Cu_2(OH)_3Cl$ system (botallackite–atacamite–
956 clinoatacamite). Structural Chemistry, 28, 153-159.
957 Koshlyakova N.N., Pekov I.V., Vigasina M.F., Zubkova N.V., Agakhanov A.A., Britvin S.N., Sidorov
958 E.G., Pushcharovsky D.Y. (2022) Reznitskyite, $CaMg(VO_4)F$, a new mineral from the Tolbachik
959 volcano, Kamchatka, Russia and the first vanadate with a titanite-type structure. Mineralogical
960 Magazine, 86, 307-313.
961 Lacroix, A. (1906) Sur quelques produit des fumerolles de la récente eruption di Vésuve et en
962 particulier sur les minéraux arsénifères et plombifères. Comptes rendus hebdomadaires des
963 séances de l'Académie des sciences, 143, 727-730.
964 Lacroix, A. (1907) Les mine aux des fumarolles de l'éruption du Vésuve en avril 1906. Bulletin de la
965 Societ française de Minéralogie et Cristallographie, 30, 219-266, Paris.
966 Liu, X.D., Hagihala, M., Zheng, X.G., Guo, Q.X. (2011) Vibrational spectroscopic properties of
967 botallackite-structure basic copper halides. Vibrational Spectroscopy, 56, 177–183.
968 Macdonald, R., Bagiński, B., Rolandi, G., De Vivo, B., Kopczyńska, A. (2016) Petrology of parasitic
969 and eccentric cones on the flanks and base of Somma-Vesuvius. Mineralogy and Petrology, 110,
970 65–85.

971 Martens, W., Frost, R.L., Williams, P. (2003) Raman and infrared spectroscopic study of the basic
972 copper chloride minerals – implications for the study of the copper and brass corrosion and
973 bronze disease. Neues Jahrbuch fur Mineralogie, Abhandlungen, 178, 197-215.
974 Mottana, A. (1998) "Vesbio" = vanadio: uno sbaglio di Arcangelo Scacchi. Memorie di Scienze
975 Fisiche e Naturali, Rendiconti della Accademia Nazionale delle Scienze, 22, 35-65.
976 Ostrooumov, M., Taran, Y. (2016) Vanadium, V – a new native element mineral from the Colima
977 volcano, State of Colima, Mexico, and implications for fumarole gas composition. Mineralogical
978 Magazine, 80, 371‑382.
979 Pekov, I.V., Zelenski M.E., Yapaskurt, V.O., Polekhovsky, Y.S., Murashko, M.N. (2013) Starovaite,
980 $KCu_5O(VO_4)_3$, a new mineral from fumarole sublimates of the Tolbachik volcano, Kamchatka,
981 Russia, European Journal of Mineralogy, 25, 91-96.
982 Pekov, I.V., Siidra, O.I., Chukanov, N.V., Yapaskurt, V.O., Britvin, S.N., Krivovichev, S.V., Schüller,
983 W., Ternes, B. (2015) Engelhaupite, $KCu_3(V_2O_7)(OH)_2Cl$, a new mineral species from Eifel,
984 Germany. Mineralogy and Petrology, 109, 705-711.
985 Pekov, I.V., Zubkova, N.V., Pushcharovsky, D.Yu. (2018) Copper minerals from volcanic
986 exhalations—a unique family of natural compounds: crystal chemical review, Acta
987 Crystallographica, 74, 502–518.
988 Pekov, I.V, Agakhanov, A.A., Zubkova, N.V., Koshlyakova, N.N., Shchipalkina, N.V., Sandalov, F.D.,
989 Yapaskurt, V.O., Turchkova, A.G., Sidorov, E.G. (2020a) Oxidizing-Type Fumaroles of the
990 Tolbachik Volcano, a mineralogical and geochemical unique. Russian Geology and Geophysics,
991 61, 675-688.
992 Pekov, I.V., Zubkova, N.V., Yapaskurt, V.O., Polekhosky, Y.S., Britvin, S.N., Turchkova, A.G.,
993 Sidorov, E.G. (2020b) Kainotropite, $Cu_4Fe^{3+}O_2(V_2O_7)(VO_4)$, a new mineral with a complex

994 vanadate anion from fumarolic exhalations of the Tolbachik Volcano, Kamchatka, Russia. The
995 Canadian Mineralogist, 58, 155-165.
996 Pekov, I.V., Koshlyakova, N.N., Zubkova, N.V., Krzątała, A., Galuskina, I.O., Belakovskiy, D.I.,
997 Galuskin, E.V., Britvin, S.N., Sidorov, E.G., Vapnik, Y., Pushcharovsky, D.Yu. (2022a)
998 Pliniusite, $Ca_5(VO_4)_3F$, a new apatite-group mineral and the novel natural ternary solid-solution
999 system pliniusite–svabite–fluorapatite. American Mineralogist, 107, 1626–1634.
1000 Pekov, I.V., Koshlyakova, N.N., Zubkova, N.V., Belakovskiy, D.I., Vigasina, M.V., Agakhanov, A.A.,
1001 Ksenofontov, D.A., Turchkova, A.G., Britvin, S.N., Sidorov, E.G., Pushcharovsky, D.Yu.
1002 (2022b) A natural vanadate–arsenate isomorphous series with jeffbenite-type structure: new
1003 fumarolic minerals udinaite, $NaMg_4(VO_4)_3$, and arsenudinaite, $NaMg_4(AsO_4)_3$. Minerals, 12, 850.
1004 Pekov, I.V., Agakhanov, A.A., Koshlyakova, N.N., Zubkova, N.V., Yapaskurt, V.O., Britvin, S.N.,
1005 Vigasina, M.F., Turchkova, A.G., Nazarova, M.A. (2023) Bakakinite, $Ca_2V_2O_7$, a new mineral
1006 from fumarolic exhalations of the Tolbachik volcano, Kamchatka, Russia. Mineralogical
1007 Magazine, 87, 695-701.
1008 Pelloux, A. (1927) The minerals of Vesuvius. American Mineralogist,12, 14–21.
1009 Petranikova, M., Tkaczyk, A.H., Bartl, A., Amato, A., Lapkovskis, V., Tunsu, C. (2020) Vanadium
1010 sustainability in the context of innovative recycling and sourcing development. Waste
1011 Management, 113, 521–544.
1012 Pollard, A.M., Thomas, R.G., Williams, P.A. (1989) Synthesis and stabilities of the basic copper(II)
1013 chlorides atacamite, paratacamite and botallackite. Mineralogical Magazine, 53, 557-563.
1014 Principe, C., Tanguy, J.C., Arrighi, S., Paiotti, A., Le Goff, M., Zoppi, U. (2004) Chronology of
1015 Vesuvius' activity from A.D. 79 to 1631 based on archeomagnetism of lavas and historical
1016 sources. Bullettin of Volcanology, 66, 703–724.

Reich, M., Palacios, C., Parada, M.A., Fehn, U., Cameron, E.M., Leybourne, M.I., Zúñiga, A. (2008) Atacamite formation by deep saline waters in copper deposits from the Atacama Desert, Chile: evidence from fluid inclusions, groundwater geochemistry, TEM, and ^{36}Cl data. Mineralium Deposita, 43, 663–675.

Rolandi, G., Petrosino, P., Geehin, J. (1998) The interplinian activity at Somma-Vesuvius in the last 3500 years. Journal of Volcanology and Geothermal Research, 82, 19–52.

Rosi, M., Principe, C., Vecci, R. (1993) The 1631 Vesuvius eruption. A reconstruction based on historical and stratigraphical data. Journal of Volcanology and Geothermal Research, 58, 151-182.

Ross, S.D. (1974) Sulphates and other oxy-anions of Group VI. In: V.C. Farmer (Ed.) The Infrared Spectra of Minerals, p. 423–444. The Mineralogical Society, London.

Russo, M., (2018) Fumarolic minerals at Vesuvius after the March 1944 eruption. Conferenza Gruppo Mineralogico Geologico Napoletano, 23 novembre 2018, p. 104.

Russo, M., Campostrini, I. (2008) Storia termica di una fumarola del Vesuvio (Campania, Italy) attraverso lo studio di minerali presenti su di un microcampione. Quaderni di Geofisica, INGV, 52, 1-9.

Russo, M., Campostrini, I. (2011) Ammineite, matlockite and post 1944 eruption fumarolic minerals at Vesuvius. GeoItalia 2011, Torino 19-23 ottobre. Plinius, 37, 312.

Russo, M., Campostrini, I., (2021). Elenco delle specie minerali del Somma-Vesuvio. Miscellanea INGV, 65, 1-36.

Russo, M., Punzo, I. (2004) I Minerali del Somma-Vesuvio. Associazione Micromineralogica Italiana Ed., Cremona, p. 320.

Russo, M., Campostrini, I., Chiappino, V.L., Punzo, I. (2009) Nuove specie minerali al Monte Somma: II. Wulfenite. Micro, periodico dell'Associazione Micromineralogica Italiana, 2, 175-176.

Russo, M., Campostrini, I., Castellano, F. (2011) Ritrovamento di atacamite in cristalli al Vesuvio. Micro, 9, 62–63.

Santacroce, R., Ed. (1987) Somma-Vesuvius. Quaderni de "La Ricerca Scientifica", 114, p. 230.

Santacroce, R., Cioni, R., Marianelli, P., Sbrana, A., Sulpizio, R., Zanchetta, G., Donahue, D.J., Joron, J.L. (2008) Age and whole rock-glass compositions of proximal pyroclastics from the major explosive eruptions of Somma-Vesuvius: A review as a tool for distal tephrostratigraphy. Journal of Volcanology and Geothermal Research, 177, 1-18.

Sbrana, A., Cioni, R., Marianelli, P., Sulpizio, R., Andronico, D., Pasquini, G. (2020) Volcanic evolution of the Somma-Vesuvius Complex (Italy). Journal of Maps, 16(2), 137-147.

Scacchi, A. (1879) Ricerche chimiche sulle incrostazioni gialle della lava vesuviana del 1631. Atti della Reale Accademia delle Scienze fisiche e matematiche, Napoli, 8, 10, 1-15.

Scacchi, A. (1880a) Ricerche chimiche sulle incrostazioni gialle della lava vesuviana del 1631. Memoria Prima. Atti della Regia Accademia delle scienze fisiche e matematiche di Napoli, 8(10), 5-19.

Scacchi, A. (1880b) Sulle incrostazioni gialle della lava vesuviana del 1631. Comunicazione. Atti della Regia Accademia dei Lincei, s. 3 Transunti, 4, 150-151.

Scacchi, A. (1882) Della lava vesuviana del 1631. Memoria Prima. Memorie di Matematica e Fisica della Società Italiana delle Scienze, s. 3, 4(8), p. 34.

Scacchi, A. (1890) Appendice alla prima Memoria sulla lava vesuviana del 1631. Memorie di Matematica e Fisica della Società Italiana delle Scienze, s. 3, 7, p. 24.

Shchipalkina, N.V., Pekov, I.V., Koshlyakova, N.N., Britvin, S.N., Zubkova, N.V., Varlamov, D.A. and Sidorov, E.G. (2020) Unusual silicate mineralization in fumarolic sublimates of the Tolbachik volcano, Kamchatka, Russia – Part 1: Neso-, cyclo-, ino- and phyllosilicates. European Journal of Mineralogy, 32, 101–119.

Schmidt, M., Lutz, H.D. (1973) Hydrogen bonding in basic copper salts: a spectroscopic study of malachite, $Cu_2(OH)_2CO_3$, and brochantite, $Cu_4(OH)_6SO_4$. Physics and Chemistry of Minerals, 20, 27 – 32.

Siidra, O.I., Borisov, A.S., Charkin, D.O., Depmeier, W., Platonova, N.V. (2021) Evolution of fumarolic anhydrous copper sulfate minerals during successive hydration/dehydration. Mineralogical Magazine 85, 262–277.

Sillitoe, R.H. (2005) Supergene oxidized and enriched porphyry cop- per and related deposits. In: Hedenquist, J.W., Thompson, J.F.H., Goldfarb, R.J., Richards, J.P. (Eds) Economic geology one hundredth anniversary volume, 1905–2005. Economic Geology Publishing Co., Littleton, Colorado, p 723–768.

Sillitoe, R.H., Rodríguez, G. (2022) Exhalative red-bed copper mineralization in travertine, Puna Plateau, northwest Argentina. Mineralium Deposita, 58, 243-261.

Solecka, U., Bajda, T., Topolska, J., Zelek-Pogudz, S., Manecki, M. (2018) Raman and Fourier transform infrared spectroscopic study of pyromorphite-vanadinite solid solutions. Spectrochimica Acta Part A: Molecular and Biomolecular Spectroscopy, 190, 96–103.

Stoilova, D., Koleva, V., Vassileva, V. (2002) Infrared study of some synthetic phases of malachite $Cu_2(OH)_2CO_3$–hydrozincite $Zn_5(OH)_6(CO_3)_2$ series. Spectrochimica Acta A, 58, 2051 – 2059.

Takahashi, H., Maehara, I., Kaneko, N. (1983) Infrared reflection spectra of gypsum. Spectrochimica Acta, 39A, 449–455.

Tao, W., Liu, X., Zheng, X., Meng, D., Guo, Q. (2011) Mid-IR and Raman spectral properties of geometrically frustrated atacamite hydroxyl copper chloride. Advanced Materials Research, 146-147, 972-975.

U.S. Geological Survey (2023) Mineral commodity summaries 2023. U.S. Geological Survey, 210 p.

U.S. Geological Survey (2022) Final List of Critical Minerals. Federal Register 87 FR 10381.

Von Raden, H.V.R., Dicks, L.W.R. (1967) Descloizite, mottramite, and vanadinite from South West Africa: an infrared and X-ray study. American Mineralogist, 52, 1067–1076.

Warr, L.N. (2021) IMA–CNMNC approved mineral symbols. Mineralogical Magazine, 85, 291-320.

Zambonini, F. (1910) Mineralogia vesuviana. Real Accademia delle scienze fisiche e matematiche, s2, 14, 368.

Zambonini, F., Carobbi, G. (1927) A chemical study of the yellow incrustations on the Vesuvian lava of 1631. American Mineralogist, 12, 1-10.

Zapol', B.A., Alksnis, F.F. (1977) Study of gypsum varieties by methods of vibrational spectroscopy. Journal of Applied Spectroscopy, 27, 1346–1351.

Zhao, Y., Cui, H., Zhang, J., Ma, Y., Tian, H., Wu, L., Cui, Q., Ma, Y. (2020) Pressure-induced phase transformation of botallackite α-$Cu_2(OH)_3Cl$ with a two-dimensional layered structure synthesized via a hydrothermal strategy. Journal of Physical Chemistry C, 124, 9581–9590.

Zhitova, E.S., Anikin, L.P., Sergeeva, A.V., Ismagilova, R.M., Rashidov, V.A., Chubarov, V.M., Kupchinenko, A.N. (2021) Volborthite occurrence at the Alaid Volcano (Atlasov Island, Kuril Islands, Russia). Geology of Ore Deposits, 63, 7, 735-748.

FIGURE CAPTIONS

Figure 1. Selected vesbine-bearing samples from the Vesuvian collection of the RMMN. (a) C26. (b) P2. (c) P9. (d) P18. (e) 902R. (f) 911R-g. (g) 912R. (h) 1002R. Size of the scale bar in the figures is 2 cm.

Figure 2. Micrographs of selected RMMN samples under polarizing optical microscopy (N//). (a) Sample C26, azurite on atacamite needles. (b) Sample C26, mixed atacamite and malachite, with late azurite. (c) Sample C26, atacamite surrounding rounded mottramite concretions. (d) Sample P2, volborthite and vanadinite. (e) Sample P18, acicular atacamite with mixed vanadinite and wulfenite-stolzite. (f) Sample P18, zoned mottramite concretions and a Mn-Cu-rich phase. (g) Sample 902R, volborthite concretions. (h) Sample 911R-a, volborthite with tiny vanadinite crystals, and thin tabular individuals of gypsum. (i) Sample 911R-a, volborthite-rich crust with few gypsum crystals. (j) Sample 990R, atacamite concretions. (k) Sample 998R, complex and strongly zoned concretions mainly composed of mottramite, vanadinite, atacamite, malachite and wulfenite-stolzite. (l) Sample 998R, as in (k), higher magnification. (m) Sample 1000R-1, concretions of volborthite with vanadinite and wulfenite-stolzite. (n) Sample 1000R-1, as in (m), at higher magnification. (o) Sample 1000R-1, as in (n), higher magnification. (p) Sample 1002R, complex and strongly zoned concretions of mottramite and volborthite. (q) Sample 1002R, as in (p), higher magnification. (r) Sample 1002R, as in (q), strongly zoned concretions of mottramite and volborthite with atacamite. Symbols as in Table 2.

Figure 3. SEM-BSE micrographs of samples of Group I (thin sections and unpolished grains). (a) Sample P2, texture consisting of zoned rosettes of volborthite, with dark green core of Vbo-1 and light green rim of Vbo-2. (b) Sample P10, platy aggregates of volborthite crystals (unpolished fragments). (c) Sample 902R, colloform aggregates composed of a Mn-V-Cu-Al-Si-Cl phase. (d) Sample 902R, as in (c) and with acicular volborthite rims. (e) Sample 902R, acicular volborthite growing on Mn-V-Cu-Al-Si-rich nuclei. (f) Sample 902R, close-up of the textures illustrated in (e). (g), (h) Sample 911R-g, euhedral hexagonal prisms of vanadinite, and reniform aggregates of subparallel platy mottramite crystals partly replacing vanadinite. (i) Sample 911R-g, mottramite

irregular grains and patinas partly surrounding stolzite-wulfenite crystals. (j) Sample 911R-g, massive atacamite with chrysocolla fillings. (k), (l) Sample 911R-b, radial fibrous aggregates of volborthite crystals, growing on a more microcrystalline volborthite core, with tiny layers of a Pb-rich phase (white parts) between them. (m), (n) Sample 911R-b, acicular crystals of Cu-vanadate with K as well (Sro-like? See text). The chemical analyses of specific spots/areas indicated in the micrographs are shown in yellow. Symbols as in Table 2 (Lct = leucite; Cpx = clinopyroxene).

Figure 4. SEM-BSE micrographs of samples of Group II (thin sections). (a) Sample C26, atacamite and azurite. (b) Sample C26, cuprite crystals surrounded by volborthite and later atacamite. (c) Sample P9, colloform and zoned texture consisting of volborthite, embedded in a V-Cu-Cl-Mn-bearing matrix, and late atacamite crystals (part of atacamite could substitute botallackite, see text). (d) Sample P9, as in (c), with a second volborthite generation growing after atacamite (and/or botallackite, see text). (e) Sample P18, Cu-Pb chemical map showing the distribution of vanadinite and mottramite in a large area of the sample. (f) Sample P18, zoned mottramite concretions with vanadinite core. (g) Sample P18, mottramite and vanadinite with banded texture of a Mn-Cu-Si-Al-V-bearing matrix. (h) Sample P18, strongly zoned colloform texture of atacamite and a mixed phase (likely vanadate-silicate). (i) Sample P18, alkali feldspar tabular crystals with radiating crystals of atacamite and stolzite-wulfenite crystals. (j) Sample 9111R-t, stolzite-wulfenite crystals followed by mottramite and late azurite. (k) Sample 912R, banded texture, with early stolzite-wulfenite, atacamite, malachite chrysocolla. (l), (m), (n), (o) Sample 998R, concentric to colloform masses of vanadinite, mottramite, malachite and mixed phases. (p) Sample 998R, enlargement of the green frame in (o). The chemical analyses of specific

spots/areas indicated in the micrographs are shown in yellow. Symbols as in Table 2 (Afs = alkali feldspar).

Figure 5. SEM-BSE micrographs of samples of Group II (thin sections). (a) Sample 1000R-1, zoned bands of vanadinite cluster surrounded by bands of mixed mottramite and a V-Cu-Mn-Zn-K-bearing phase. (b) Sample 1000R-1, euhedral stolzite-wulfenite crystal with a thin layer of mottramite and a Cu-Mn-Si-Al-V phase. (c), (d), (e) Sample 1002R, rhythmic colloform texture of mottramite, volborthite and atacamite aggregates. (f), (g), (h), (i) Sample 1002R, chemical maps with distribution of Pb, V, Cl and Cu, respectively. (j) Sample 1002R, another part of the investigated area with distinct colloform layers. (k), (l), (m), (n), (o) Sample 1002R, chemical maps of Pb, Cl, V, Cu and Si, respectively. The chemical analyses of specific areas indicated in the micrographs are shown in yellow. Symbols as in Table 2.

Figure 6. TEM-HRTEM-SAED-EDS data of selected Group I samples. (a) Sample 902R. HAADF (top left) and textural (top center) images of volborthite fragments; HRTEM image (top right) of area indicated by the sky-blue arrow in the textural image, with white lattice fringes corresponding to 5.2 Å spacings (200), and the SAED (inset) showing a diffuse ring pattern and a reflections at ca. 5 Å (110); three selected chemical maps (bottom left) of volborthite grain showed in the textural image; EDS spectrum (bottom right) of volborthite (Area #1, yellow frame in the left map), having small amounts of Zn, as well as traces of Si and Al (hereafter the Au peaks visible in the EDS spectra come from to the gold grids used for TEM sample preparation). (b) Sample 911-R. Textural image (top left) of mixed mottramite, chrysocolla vanadinite polycrystalline particles, locally showing very fine-grained rounded concretions; HRTEM (top center) image referring to area of the sky-blue arrow in the textural image, with 8.9 Å lattice

fringes of vanadinite (100), and the corresponding SAED pattern (inset); chemical map (top right) of the fragments in the textural image, indicating the Cu-Cl distribution; EDS spectra of mottramite (referring to Area #1 in the upper map), which displays trace amounts of As, Al, Si, Cl and Zn, and vanadinite (Area #2 in the upper map), with traces of As. Symbols as in Table 2.

Figure 7. TEM-HRTEM-SAED-EDS data of Group II samples. (a) Sample P9. Textural (bright-field) image of volborthite-rich particle with HRTEM volborthite image (top left) showing 3 Å spacings corresponding to (-112) and the SAED image of single crystal ring pattern (inset), taken in the area with the sky-blue arrow in the textural image; textural image of polycrystalline grain with HRTEM image (top right) of crystalline patches with lattice fringe (area with the sky-blue arrow in the textural image) corresponding to 5.3 Å spacings of volborthite (200), and SAED image (inset) of polycrystalline ring pattern; Cu-Cl and Cu-Si chemical maps (bottom left) of the particles in top right; EDS spectrum of Area #1 in the top right image, referring to volborthite with small contents of Mn, Si, Al, and As. (b) Sample P18. Textural image of triangular vanadinite crystal, together with a volborthite-prevailing particle, and vanadinite HRTEM image of (sky-blue arrow area in the textural image) showing lattice fringe related to 3.4 Å spacing (102), with the corresponding SAED pattern in the inset [3.3 Å, (210), (012)] (top left); chemical maps of Cu-Si-V (top right) and Mn (bottom left) of the upper left particles; EDS spectra (center and right bottom) of Areas #1 and #2 in top left textural image, showing vanadinite with small contents of As, Si, K and Cu, as well as a Cu-Mn rich phase (see text). (c) Sample 1002R. HAADF image and Cu-Pb chemical map (top left) of atacamite and mottramite fragments; particle in the top left image, indicated by the green asterisk) and the related Cu-Pb chemical map (bottom left); textural image of an atacamite grain (indicated with asterisk in the HAADF image) in the HRTEM image (top right) acquired in the sky-blue arrow area, with lattice fringe

corresponding to 5 Å spacing (101) of atacamite and the related SAED (inset) pattern [5.4 Å, (011)]; EDS spectra (bottom) of atacamite and mottramite (Areas #1 and #2, respectively, in the top left HAADF image). Symbols as in Table 2.

Figure 8. Grouping spectra in the two different FTIR spectral regions. 400 – 1800 cm^{-1} region. (a) Type I spectra: azurite and malachite predominant. (b) Type II spectra: atacamite, volborthite, predominant. (c) Type III spectra: atacamite, volborthite, botallackite predominant. (d) Type IV spectra: atacamite, volborthite, chrysocolla predominant. 3000 – 3800 cm^{-1} region. (e) Type A OH spectra: atacamite predominant. (f) Type B OH spectra: atacamite predominant. (g) Type C OH spectra: azurite, malachite predominant. (g) Ungrouped OH spectra: 997R, malachite predominant; $P9_{green}$, botallackite and atacamite predominant; C5, tentatively assigned to azurite. Small peak marked with "*" in (b), (c) and (d) is an instrumental artifact or an impurity in KBr.

Figure 9. A possible paragenetic model for the studied *vesbine* assemblages (in the T range of ca. 400-100 °C; see text), hypothesized by combined OM, SEM-EDS-WDS and TEM studies. Splitting and dimensions of the bars roughly indicate different generations and abundance of minerals (phases in Italics detected by XRPD and/or FTIR).

TABLE CAPTIONS

Table 1. The investigated Somma-Vesuvius samples with V-bearing minerals from the Royal Mineralogical Museum of Naples, with mineralogical description and location as reported in the original labels (when present), as well as the type of analysis carried out for each sample.

Table 2. Main mineral associations of the investigated samples, sorted in Groups I and II, inferred by combined mineralogical analyses (mineral symbols mainly after Warr, 2021).

Table 3. Grouping spectra in the two different spectral regions.

Table 4. Bands assignments in the 400 – 1800 cm^{-1} spectral range.

Table 5. Bands assignments in the 3000 – 4000 cm^{-1} spectral range.

SUPPLEMENTAL MATERIALS

Supplementary Figures

Supplemental Figure S1. XRPD patterns of the investigated samples of Groups I and II, with the indication of the main recorded phases (sublimate minerals in bold, minerals from the lava host rock in Italics).

Supplemental Figure S2. TEM-HRTEM-SAED-EDS data of samples of Group I. (a) 902R. Volborthite grains and mixed particles; 1. Cu-Si chemical map of volborthite and volborthite-rich fragments; 2. EDS spectrum of volborthite (Area #1 in 1), with trace amounts of Zn, Si and Al; 3. EDS spectrum of a supposed mixed volborthite-silicate-oxide particle (Area #2 in 1),

1255 having small contents of Si, Al, Ca and K, as well as Mn, Ba and Zn; 4. Cu-Mn chemical map of
1256 a heterogeneous particle; 5. EDS spectrum of volborthite (Area #1 in 4), with trace content of Zn;
1257 6. EDS spectrum of Area #2 in 4, referring to the greenish-colored areas, and showing small
1258 amounts of Mn, together with Si, Al, Ca, K, Ba and Zn (mixed volborthite-silicate-oxide?). (b)
1259 and 911R-g. Chrysocolla-rich grain; 1. textural image, with darker areas and rounded structures
1260 (lower part); 2. EDS spectrum of Area #1 in 1, attributable to chrysocolla; 3. 4. 5. 6. chemical
1261 maps of the fragment in 1, with the distribution of Cu-Si, Cu-Pb, Cu-V and Cu-Cl, respectively.
1262 Symbols as in Table 2.
1263
1264 **Supplemental Figure S3.** TEM-HRTEM-SAED-EDS data of sample P9 (Group II). (a) Mixtures of
1265 volborthite, atacamite and a likely Fe oxide; 1. HAADF image; 2. EDS spectrum of Area #1 in 1,
1266 corresponding to a possible Fe(Mn,Mg,Ti) oxide with minor amounts of Cu from the surrounding
1267 particles; 3. 4. 5. 6. 7. chemical maps of Cu-Cl, Fe, Mn, Mg(+Ti), respectively. (b) Volborthite-
1268 prevailing fragments; 1. HAADF image; 2. EDS spectrum of Area #1 in 1; 3. 4. 5. 6. chemical
1269 maps of Cu-Si, Cu-Mn, Cu-Cl and As, respectively. (c) Mixed grains; 1. HAADF image; 2. 3.
1270 EDS spectra of Areas #1 and #2 in 1, respectively; 4. 5. 6. chemical maps of Cu-Mn, Cu-Cl, and
1271 Cu-V, respectively. Symbols as in Table 2.
1272
1273 **Supplemental Figure S4.** TEM-HRTEM-SAED-EDS data of samples P18 and 1002R (Group II). (a)
1274 P18. Mixed mottramite-chrysocolla grain; 1. textural image (HAADF) displaying aggregates of
1275 euhedral mottramite crystals surrounded by chrysocolla; 2. 3. 4. chemical maps of the particle in
1276 1, showing the distribution of Cu-Si, As and Mn; 5. EDS spectrum of a mixture of mottramite
1277 and chrysocolla (Area #1 in 1); 6. EDS spectrum of chrysocolla (Area #2 in 1). Symbols as in
1278 Table 2. (b) 1002R. Mottramite aggregate; 1. textural image; 2. lattice fringe image of mottramite

(referring to the area indicated by the sky-blue arrow in 1), with corresponding to 2.7 Å spacing (212), and the related SAED pattern in the inset (4.0 Å, (102); 3. HAADF chemical map with Cu-Pb distribution; 4. 5. 6. chemical map of Cu, V and Pb of mottramite, respectively; E7. EDS spectrum of mottramite (Area #1 in 3). Symbols as in Table 2.

Supplemental Figure S5. OH spectra of Type D (see text for description).

Supplementary Tables

Supplemental Table S1. Summary of minerals and their formulas cited in the text.

Supplemental Table S2. Selected compositions of volborthite from the studied samples (EDS). Sample in bold Italics were analyzed by WDS.

Supplemental Table S3. Selected compositions of mottramite from the studied samples (EDS). Sample in bold Italics were analyzed by WDS.

Supplemental Table S4. Selected compositions of vanadinite (EDS).

Supplemental Table S5. Selected compositions of atacamite from the studied samples (EDS). Sample in bold Italics were analyzed by WDS.

1303 **Supplemental Table S6.** Selected compositions of miscellaneous minerals (EDS).

1304

1305 **Supplemental Table S7.** Selected compositions of azurite and malachite from the studied samples

1306 (EDS).

1307

1308

1309

This is the peer-reviewed, final accepted version for American Mineralogist, published by the Mineralogical Society of America.
The published version is subject to change. Cite as Authors (Year) Title. American Mineralogist, in press.
DOI: https://doi.org/10.2138/am-2023-9126. http://www.minsocam.org/

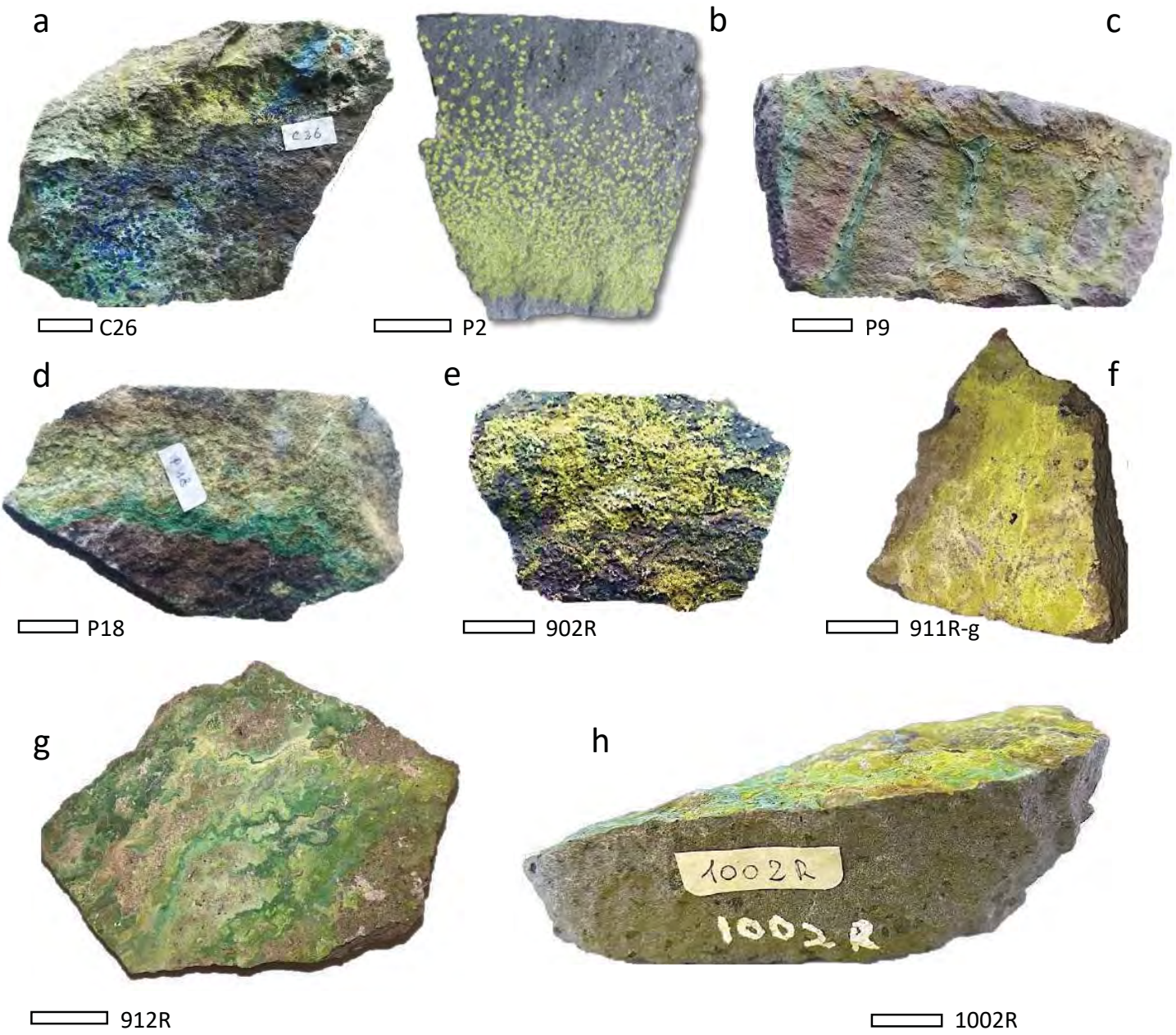

Fig. 1

This is the peer-reviewed, final accepted version for American Mineralogist, published by the Mineralogical Society of America.
The published version is subject to change. Cite as Authors (Year) Title. American Mineralogist, in press.
DOI: https://doi.org/10.2138/am-2023-9126. http://www.minsocam.org/

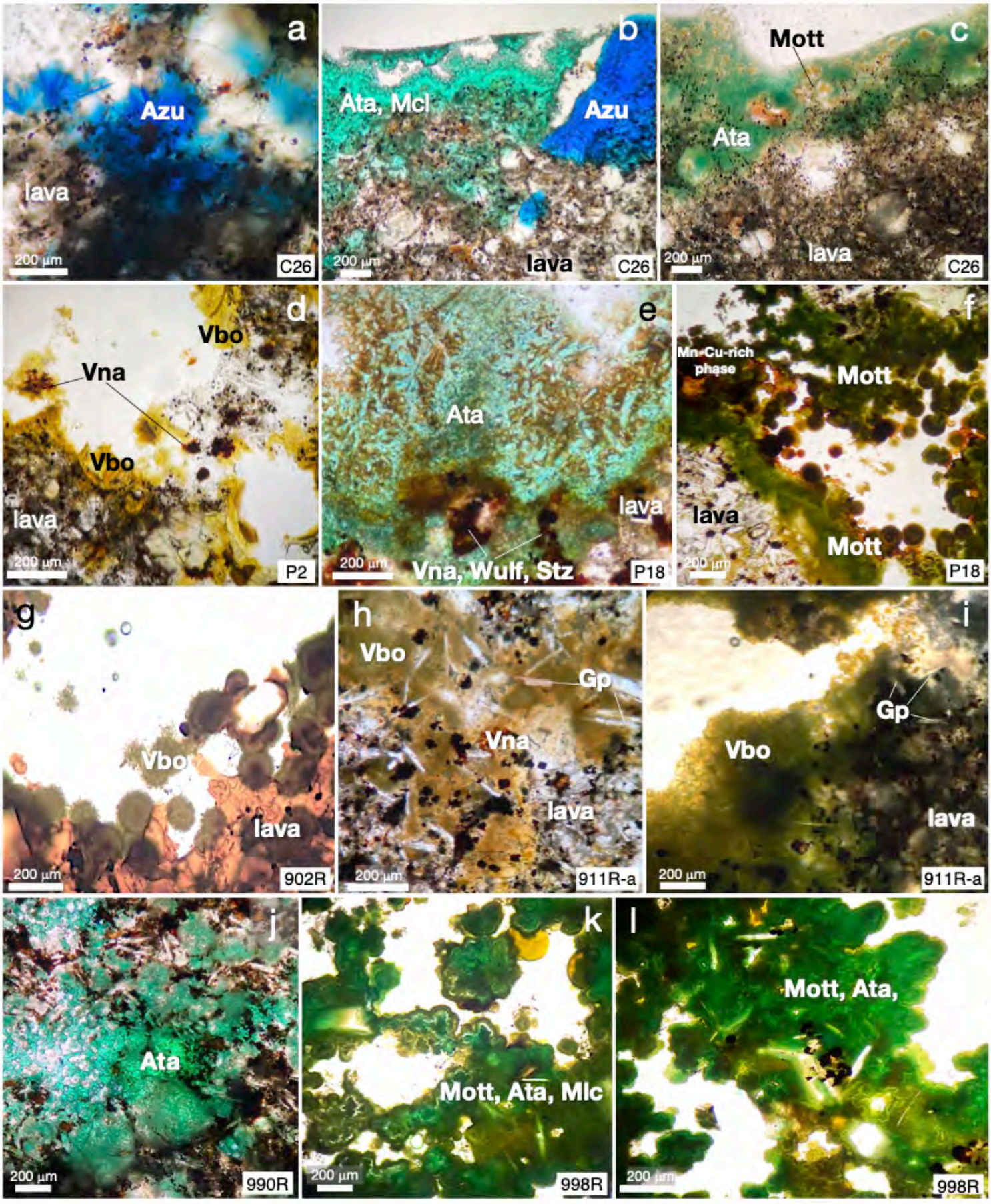

Fig. 2 (continued)

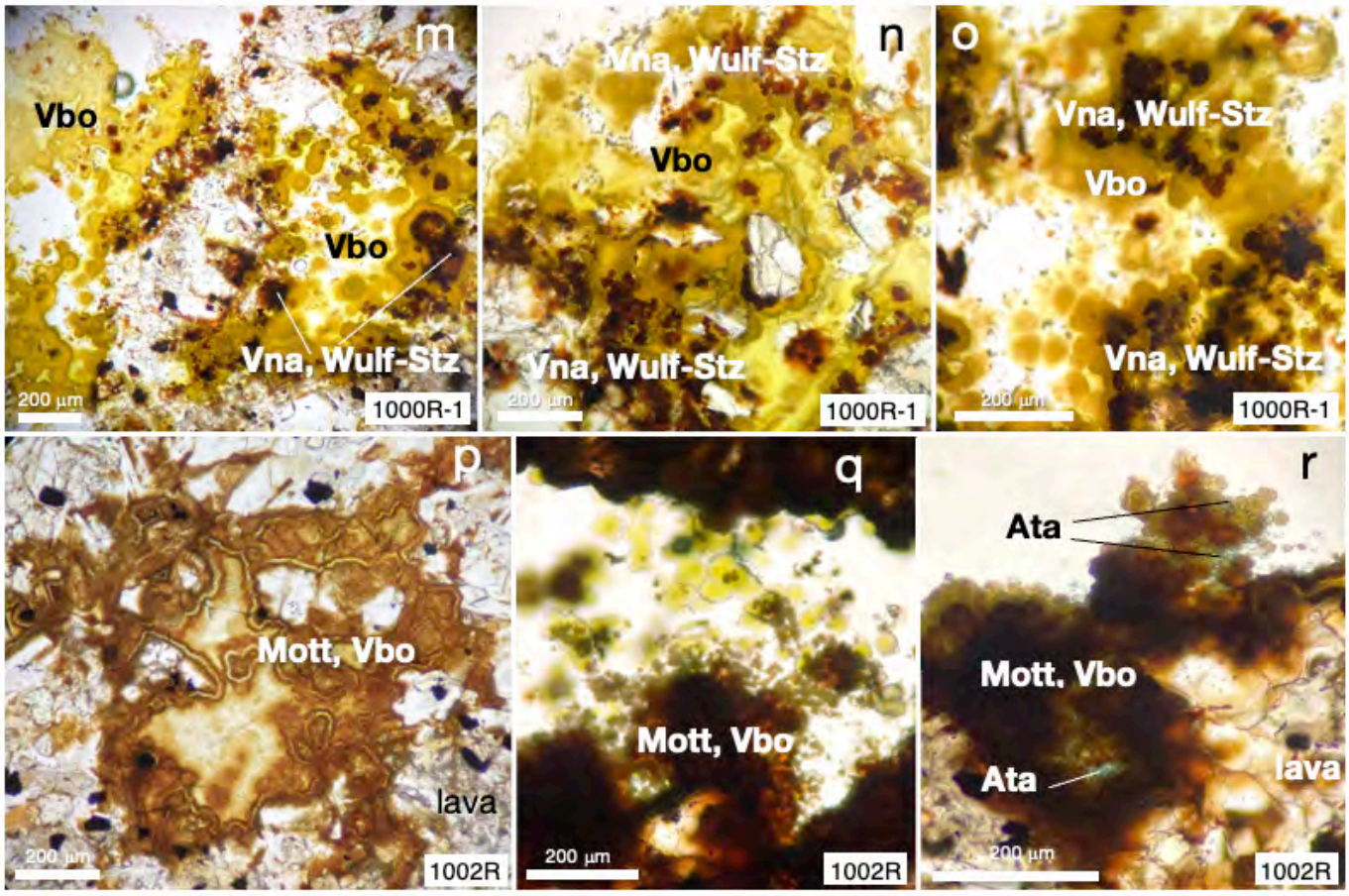

Fig. 2 (end)

This is the peer-reviewed, final accepted version for American Mineralogist, published by the Mineralogical Society of America.
The published version is subject to change. Cite as Authors (Year) Title. American Mineralogist, in press.
DOI: https://doi.org/10.2138/am-2023-9126. http://www.minsocam.org/

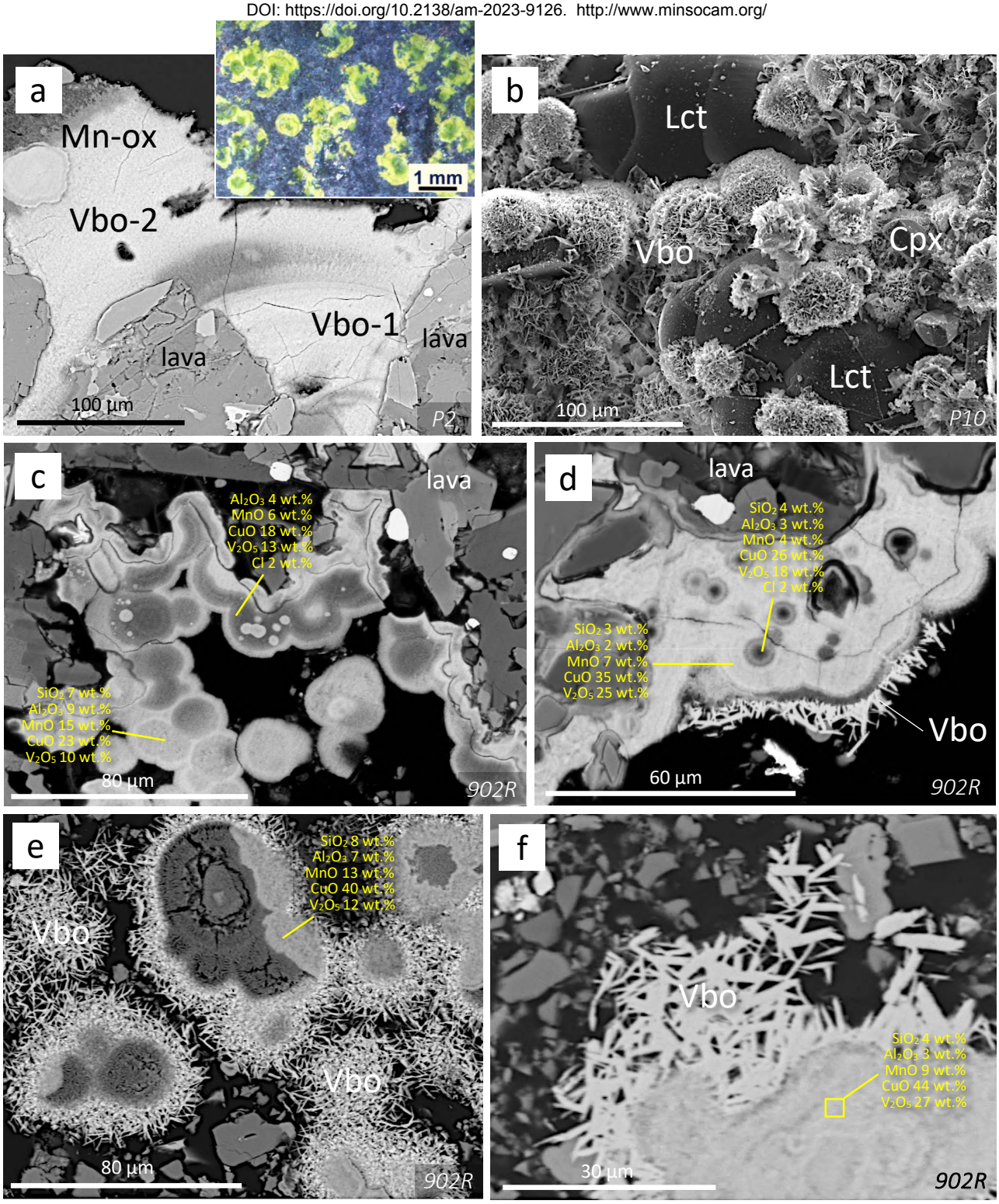

Fig. 3 (continued)

This is the peer-reviewed, final accepted version for American Mineralogist, published by the Mineralogical Society of America.
The published version is subject to change. Cite as Authors (Year) Title. American Mineralogist, in press.
DOI: https://doi.org/10.2138/am-2023-9126. http://www.minsocam.org/

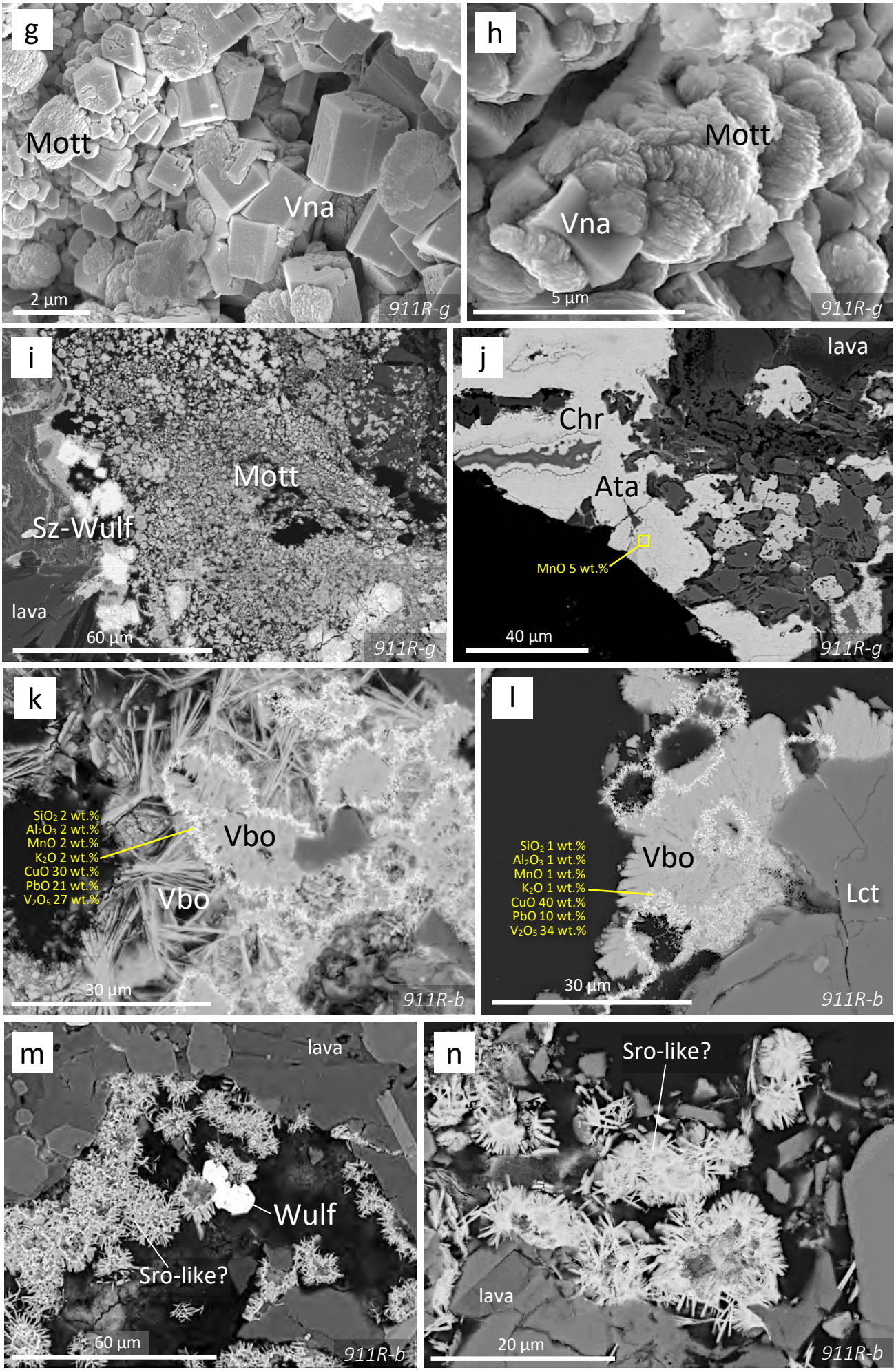

Fig. 3 (end)

This is the peer-reviewed, final accepted version for American Mineralogist, published by the Mineralogical Society of America.
The published version is subject to change. Cite as Authors (Year) Title. American Mineralogist, in press.
DOI: https://doi.org/10.2138/am-2023-9126. http://www.minsocam.org/

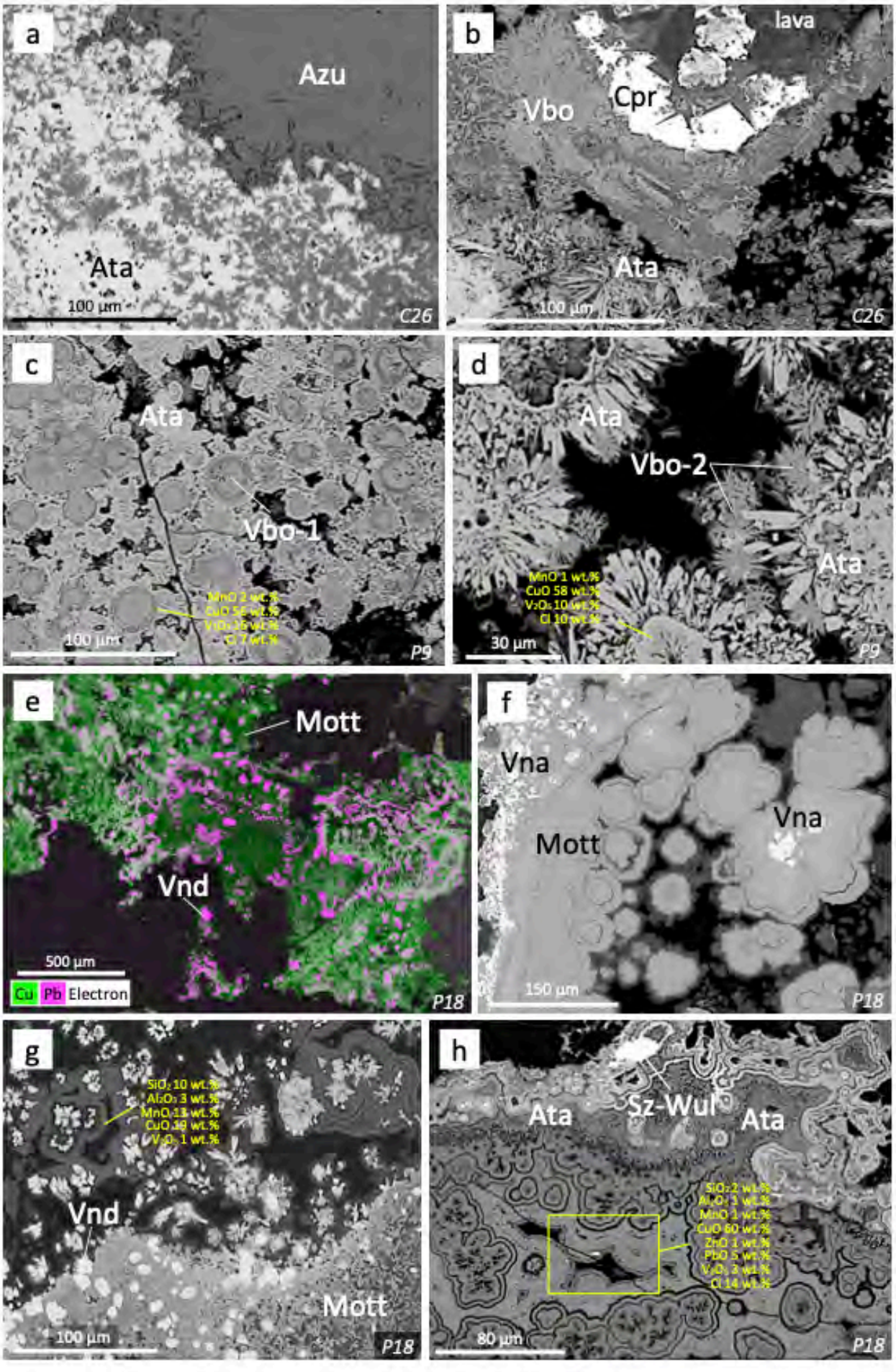

Fig. 4 (continued)

This is the peer-reviewed, final accepted version for American Mineralogist, published by the Mineralogical Society of America.
The published version is subject to change. Cite as Authors (Year) Title. American Mineralogist, in press.
DOI: https://doi.org/10.2138/am-2023-9126. http://www.minsocam.org/

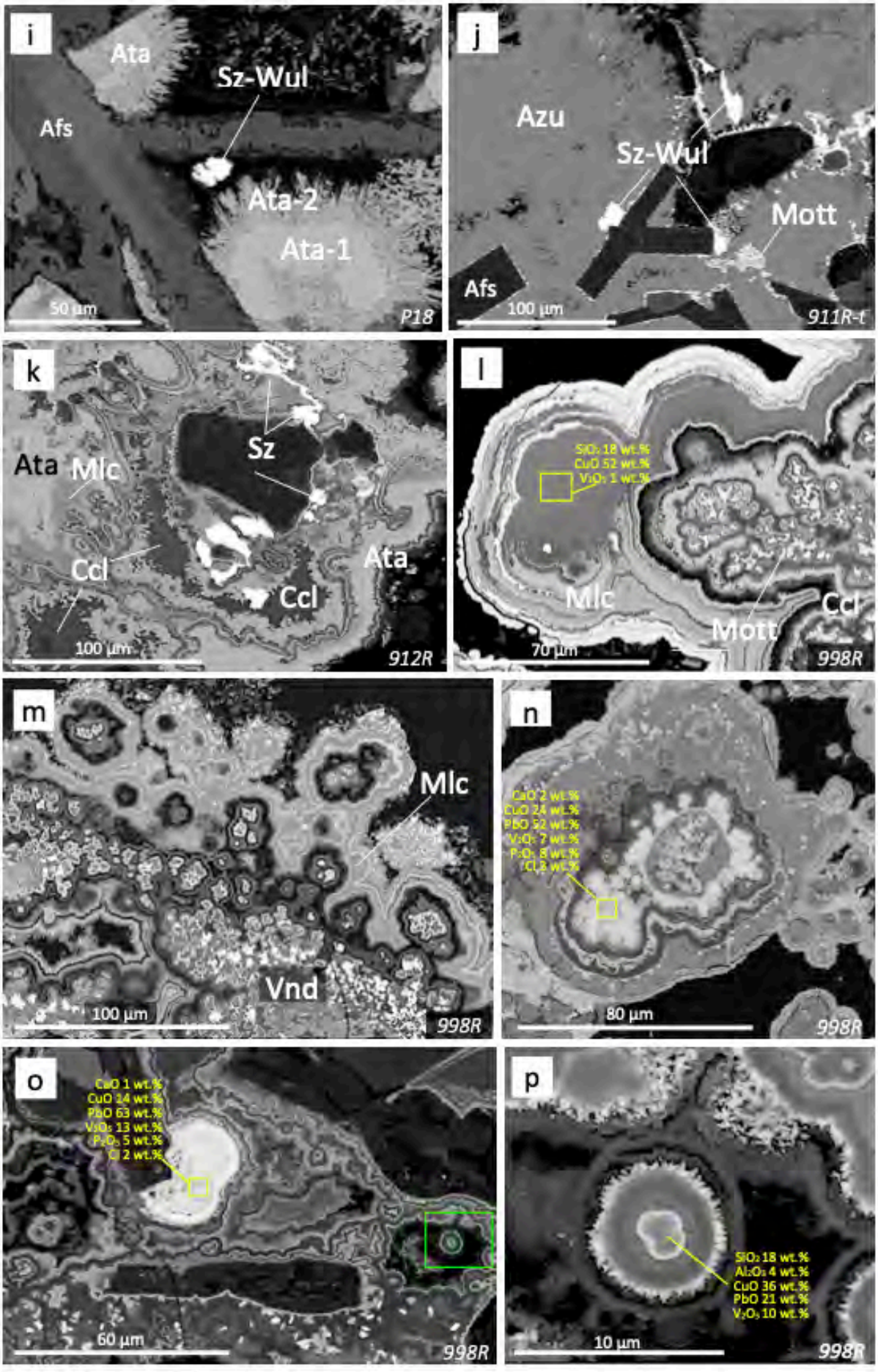

Fig. 4 (end)

This is the peer-reviewed, final accepted version for American Mineralogist, published by the Mineralogical Society of America.
The published version is subject to change. Cite as Authors (Year) Title. American Mineralogist, in press.
DOI: https://doi.org/10.2138/am-2023-9126. http://www.minsocam.org/

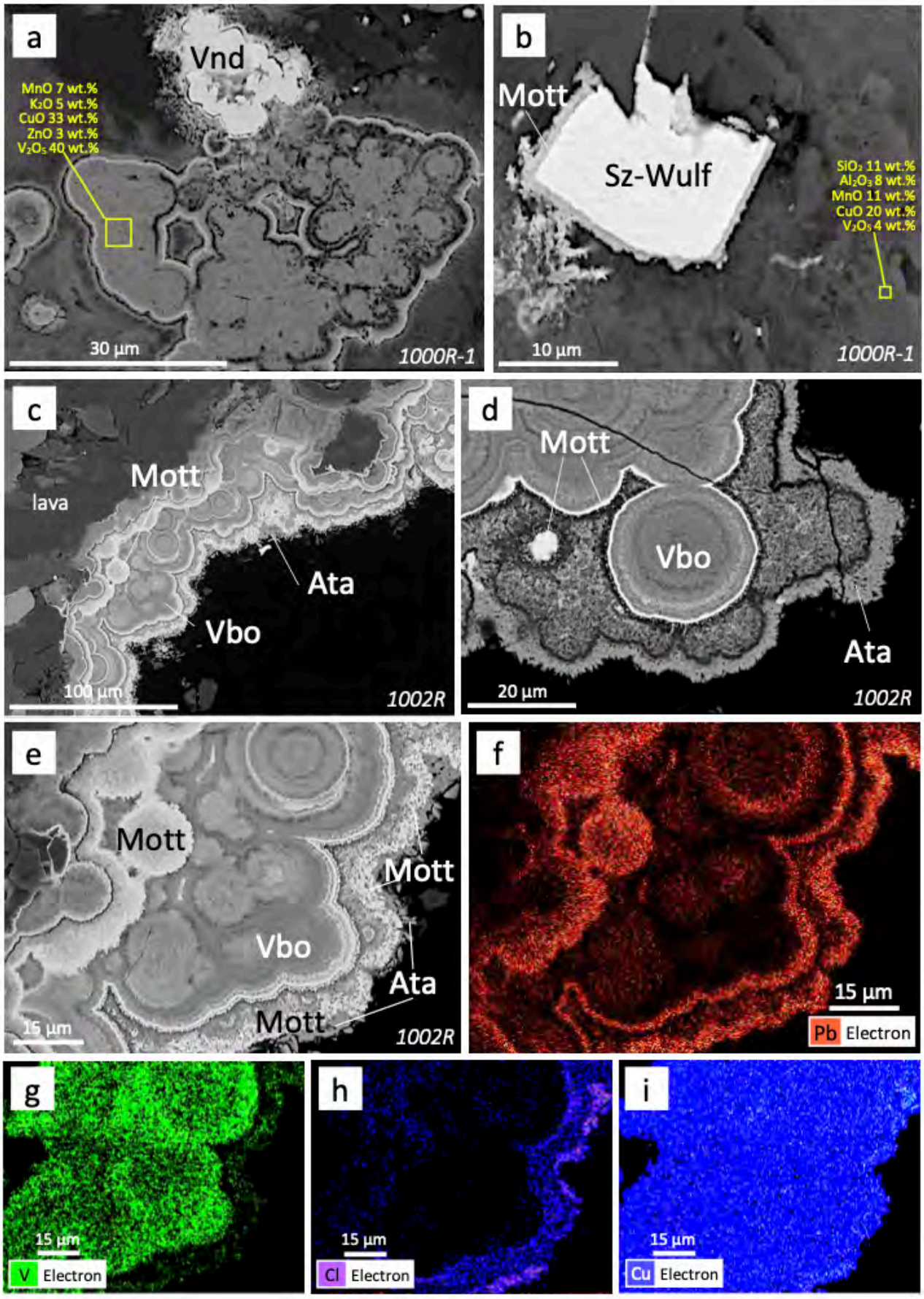

Fig. 5 (continued)

This is the peer-reviewed, final accepted version for American Mineralogist, published by the Mineralogical Society of America.
The published version is subject to change. Cite as Authors (Year) Title. American Mineralogist, in press.
DOI: https://doi.org/10.2138/am-2023-9126. http://www.minsocam.org/

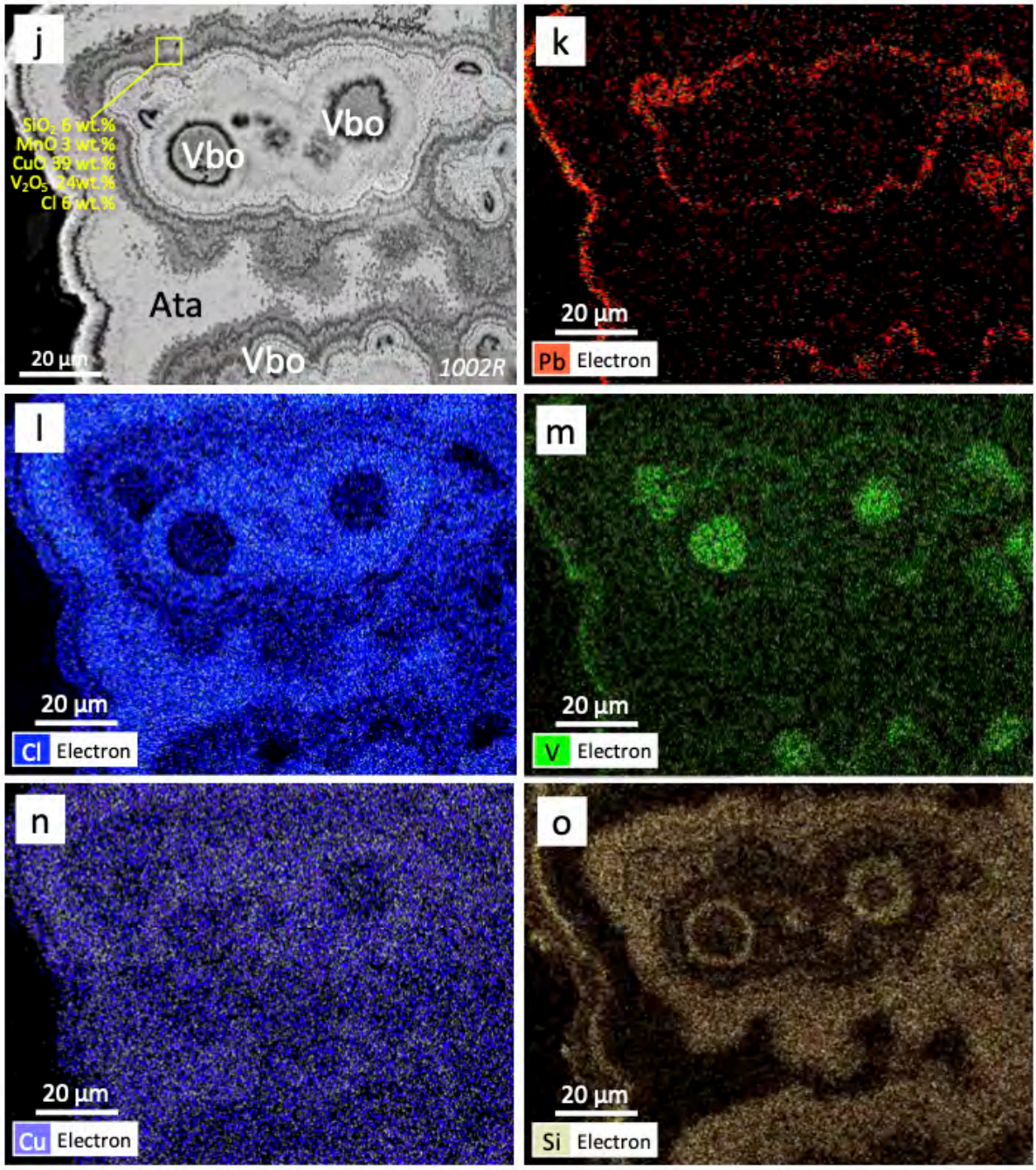

Fig. 5 (end)

This is the peer-reviewed, final accepted version for American Mineralogist, published by the Mineralogical Society of America.
The published version is subject to change. Cite as Authors (Year) Title. American Mineralogist, in press.
DOI: https://doi.org/10.2138/am-2023-9126. http://www.minsocam.org/

a

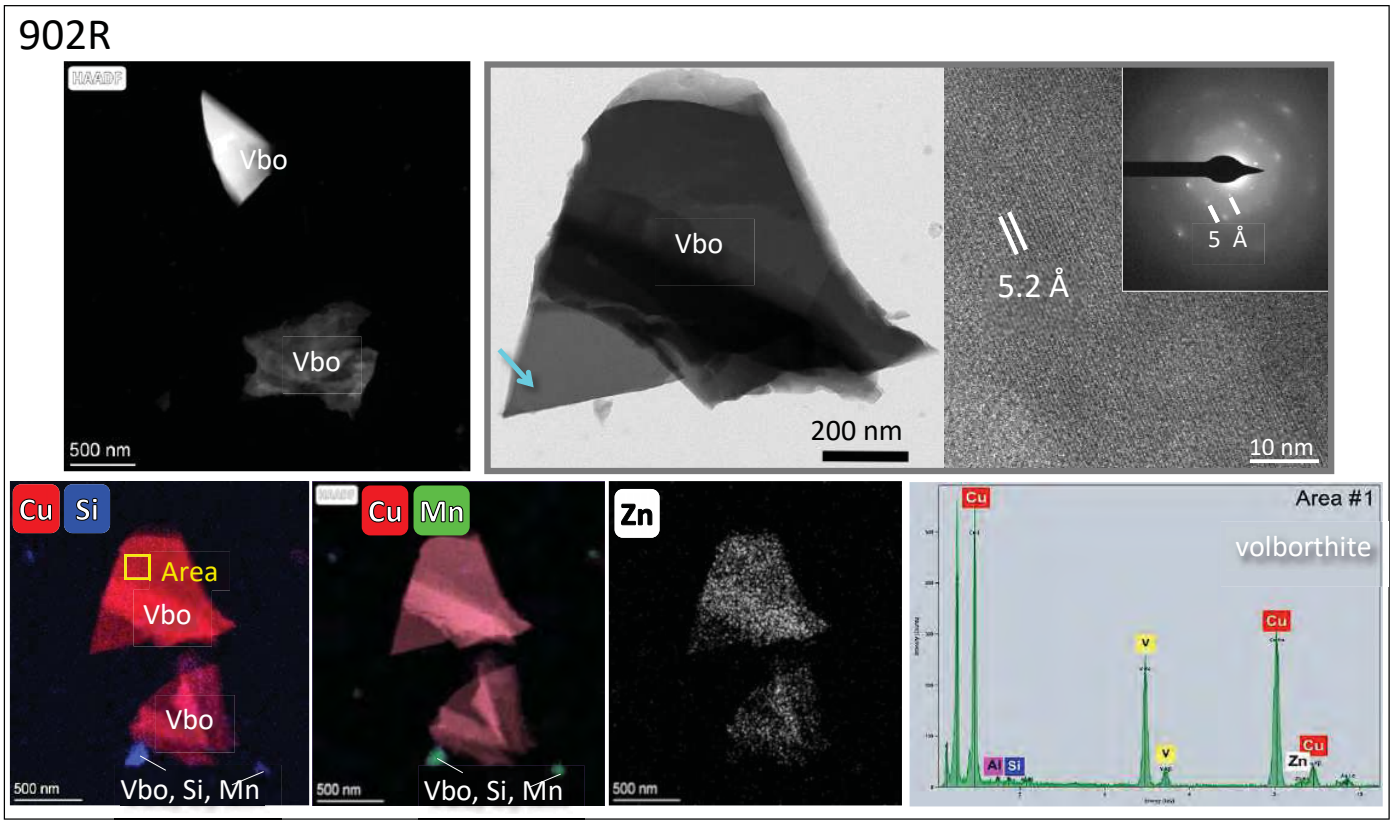

b

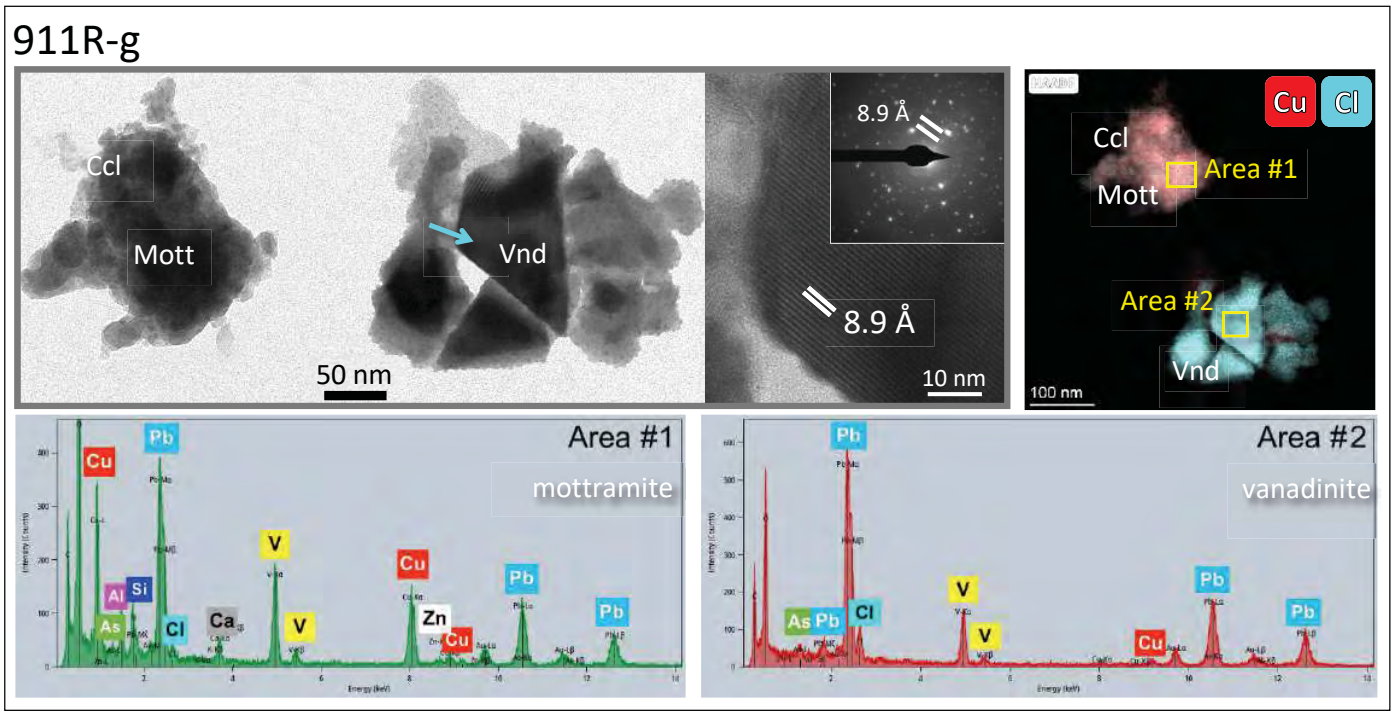

Fig. 6

This is the peer-reviewed, final accepted version for American Mineralogist, published by the Mineralogical Society of America.
The published version is subject to change. Cite as Authors (Year) Title. American Mineralogist, in press.
DOI: https://doi.org/10.2138/am-2023-9126. http://www.minsocam.org/

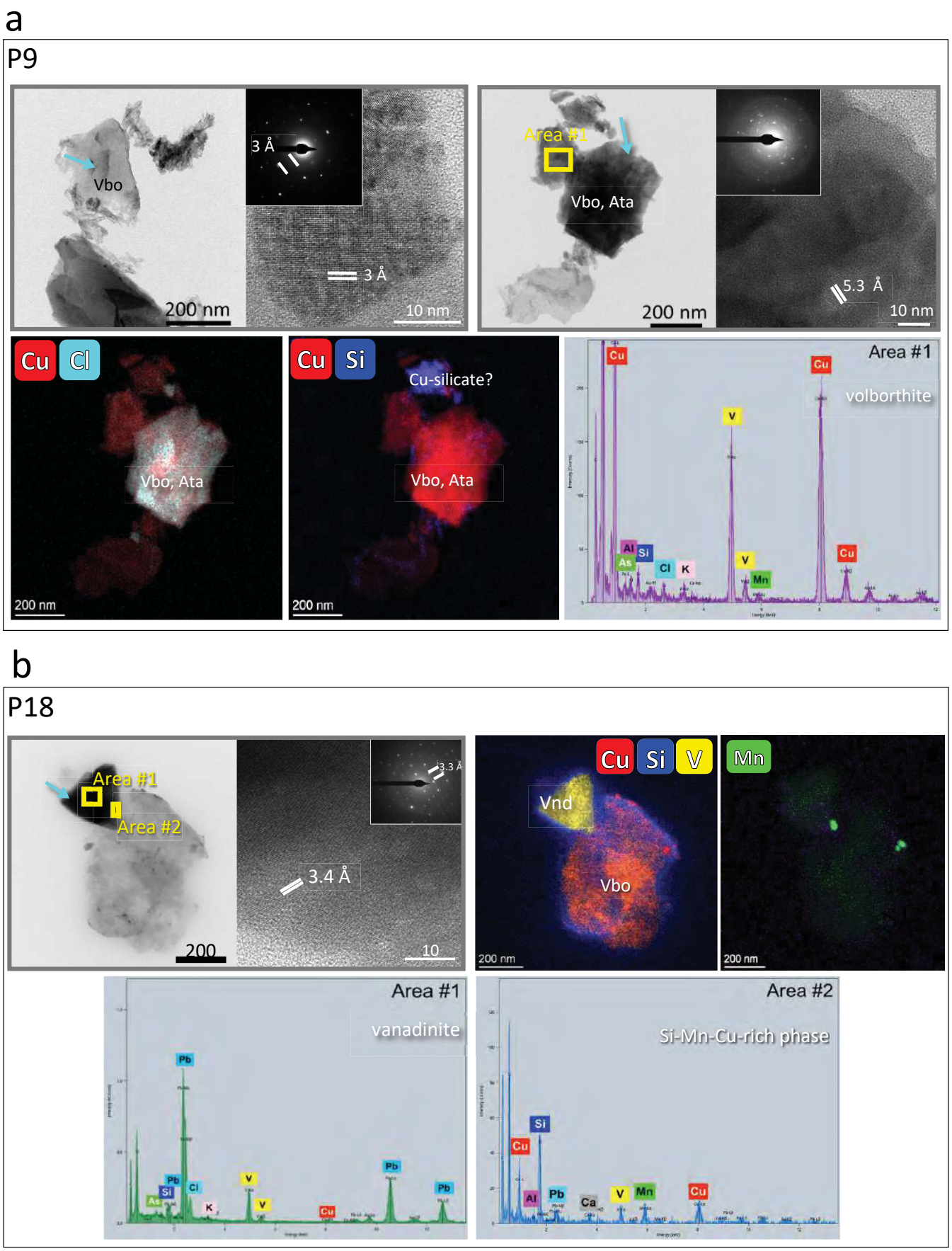

Fig. 7 (continued)

This is the peer-reviewed, final accepted version for American Mineralogist, published by the Mineralogical Society of America.
The published version is subject to change. Cite as Authors (Year) Title. American Mineralogist, in press.
DOI: https://doi.org/10.2138/am-2023-9126. http://www.minsocam.org/

C

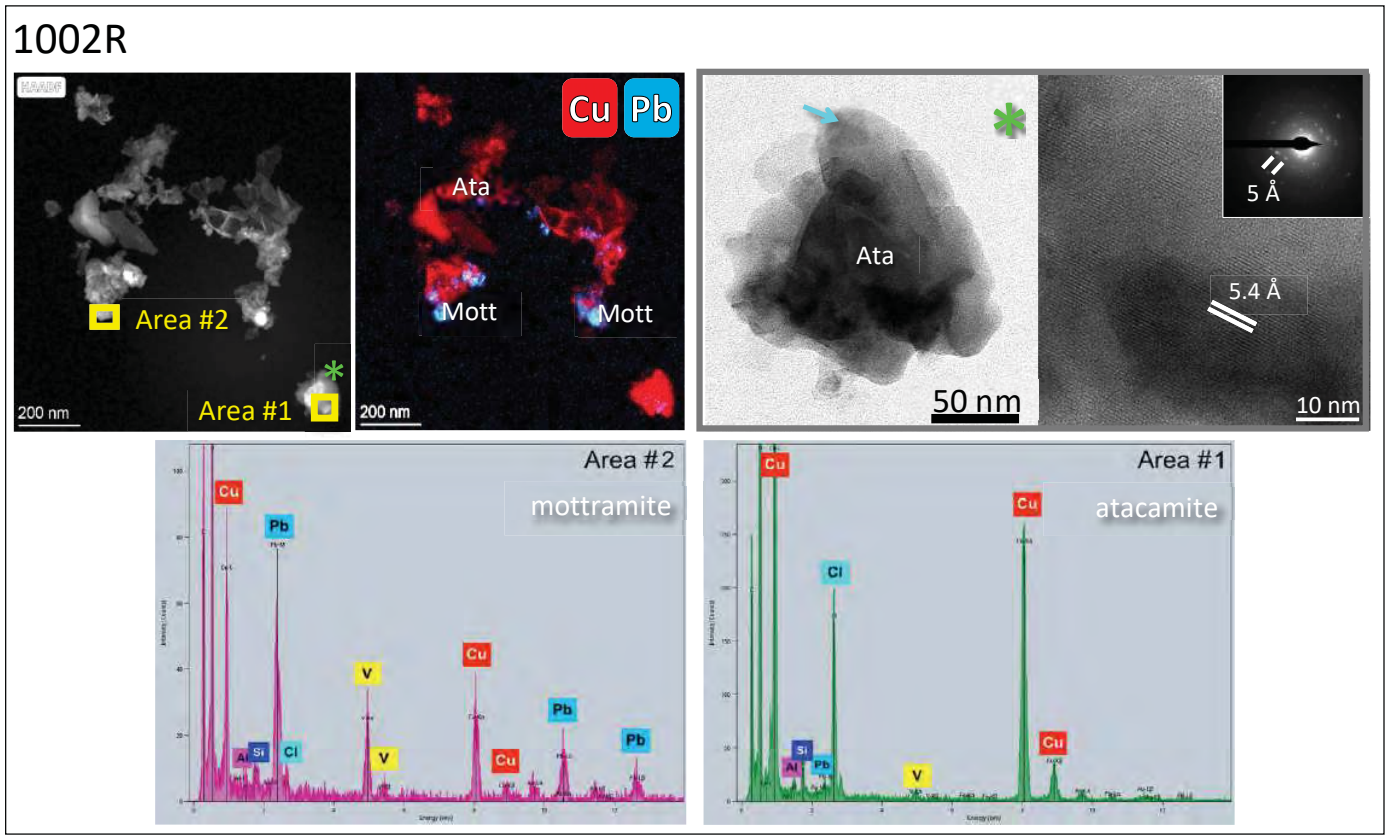

Fig. 7 (end)

This is the peer-reviewed, final accepted version for American Mineralogist, published by the Mineralogical Society of America.
The published version is subject to change. Cite as Authors (Year) Title. American Mineralogist, in press.
DOI: https://doi.org/10.2138/am-2023-9126. http://www.minsocam.org/

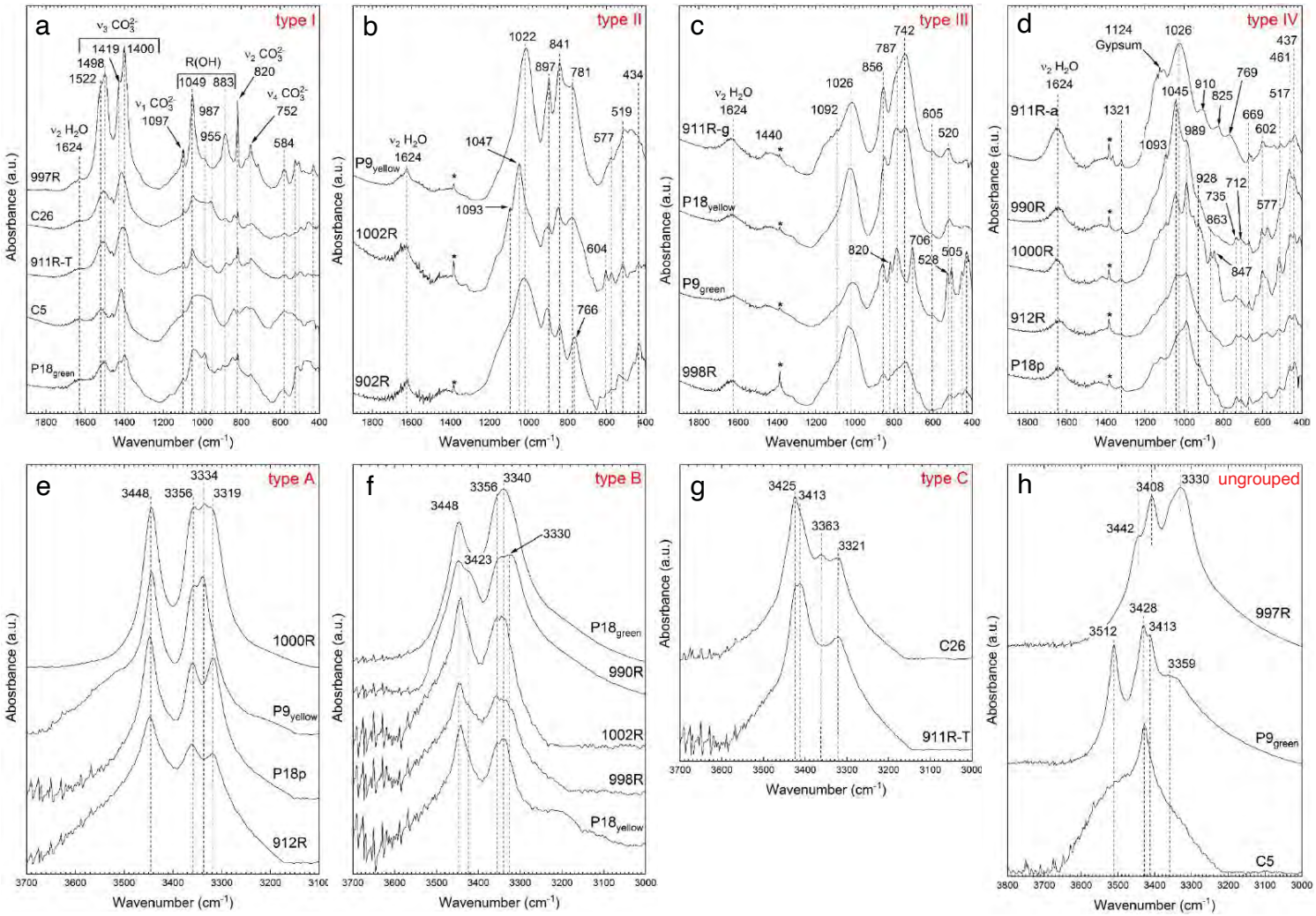

Fig. 8

This is the peer-reviewed, final accepted version for American Mineralogist, published by the Mineralogical Society of America.
The published version is subject to change. Cite as Authors (Year) Title. American Mineralogist, in press.
DOI: https://doi.org/10.2138/am-2023-9126. http://www.minsocam.org/

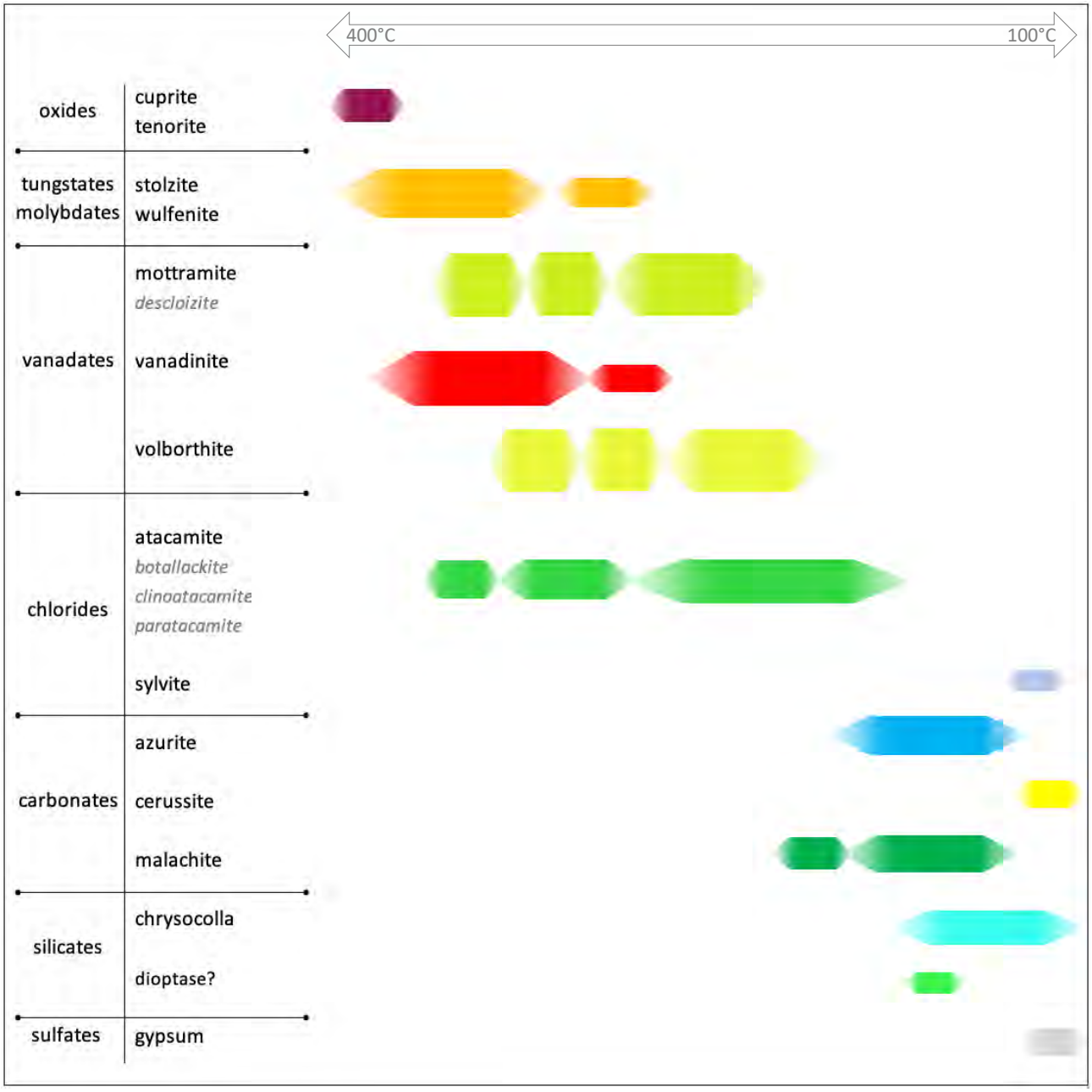

Fig. 9

This is the peer-reviewed, final accepted version for American Mineralogist, published by the Mineralogical Society of America.
The published version is subject to change. Cite as Authors (Year) Title. American Mineralogist, in press.
DOI: https://doi.org/10.2138/am-2023-9126. http://www.minsocam.org/

Table 1

The investigated Somma-Vesuvius samples with V-bearing minerals from the Royal Mineralogical Museum of Naples, with mineralogical description and location as reported in the original labels (when present), as well as the type of analysis carried out for each sample.

#	Sample ID	Museum label classification	Museum label occurrence	Analyes
1	C5	Azurite, Vesbine, Hausmannite	Vesuvius, 1631 lava (Uncino)	XRPD, SEM, FTIR
2	C26	Azurite	Vesuvius, 1631 lava	XRPD, SEM, EDS, FTIR
3	P2	Vesbine	Vesuvius, 1631 lava	XRPD, SEM, EDS
4	P8	Vesbine, Hausmannite	Vesuvius, 1631 lava	SEM, EDS
5	P9	Vesbine	-	XRPD, SEM, EDS, WDS, TEM
6	P10	Vesbine with Atacamite on Sodalite	Vesuvius, 1631 lava	SEM
7	P18	Vesbine with Atacamite	-	XRPD, SEM, EDS, WDS, TEM, FTIR
8	P18p	Vesbine with Atacamite	-	XRPD, SEM, FTIR
9	902R	-	-	SEM, EDS, WDS, TEM, FTIR
10	911R-g	Vesbine	Vesuvius, 1631 lava	XRPD, SEM, EDS, WDS, TEM, FTIR
11	911R-a	Vesbine	Vesuvius, 1631 lava	XRPD, SEM, EDS, FTIR
12	911R-b	Vesbine	Vesuvius, 1631 lava	SEM, EDS
13	911R-T	Vesbine	Vesuvius, 1631 lava	XRPD, SEM, EDS, FTIR
14	912R	-	-	XRPD, EDS, FTIR
15	984R			XRPD, SEM, EDS
16	990R	-	-	XRPD, SEM, EDS, FTIR
17	990R-2	-	-	SEM
18	997R	-	-	XRPD, SEM, EDS, FTIR
19	998R	-	Vesuvius, 1631 lava (Camaldoli)	XRPD, EDS, FTIR
20	1000R-1	-	-	SEM, EDS, FTIR
21	1001R	-	-	SEM
22	1002R	-	-	XRPD, EDS, TEM, FTIR
23	11232 D1684	Azurite with Vesbine and Atacamite	-	SEM

This is the peer-reviewed, final accepted version for American Mineralogist, published by the Mineralogical Society of America.
The published version is subject to change. Cite as Authors (Year) Title. American Mineralogist, in press.
DOI: https://doi.org/10.2138/am-2023-9126. http://www.minsocam.org/

Table 2
Main mineral associations of the investigated samples, sorted in Groups I and II, inferred by combined mineralogical analyses (mineral symbols mainly after Warr, 2021).

Sample ID	Group*	Angle site	Ataca mite	Azur ite	Botalla ckite	Cerus site	Chryso colla	Clinoatac amite	Cupr ite	Descloi zite	Diopt ase	Fe-oxi-hydrox ides	Gyps um	Malac hite	Mn-oxi-hydroxid es	Mottra mite	Parataca mite	Starov aite	Stolzite ***	Sylv ite	Teno rite	Vanadi nite	Volbort hite	Wulfe nite
	**	Ang	**Ata**	**Azu**	Blk	Cer	**Ccl**	Cata	**Cpr**	Dcz	Dpt	Fe-ox	Gp	**Mlc**	Mn-ox	**Mott**	Pata	**Sro-like**	**Sz**	Syl	Tnr	**Vna**	**Vbo**	**Wul**
P2	I											o			o							o	o	
P8	I															o						o	o	
P10	I		o																				o	
902R	I														o								o	
911R-g	I		o				o			o						o			o			o		o
911R-a	I		o										o							o		o	o	
911R-b	I					o										o		o					o	o
990R-2	I		o																				o	
1001R	I																						o	
C5	II		o	o		o										o						o		o
C26	II		o	o					o					o		o						o	o	
P9	II		o		o			o	o	o													o	
P18	II		o				o	o		o		o			o	o			o			o	o	o
P18p	II		o				o									o	o		o				o	
911R-T	II		o	o										o		o			o			o		o
912R	II		o				o							o			o		o			o		
984R	II	o	o				o					o					o						o	
990R	II		o	o										o								o		
997R	II													o		o	o		o			o		
998R	II		o							o	o			o	o	o			o		o	o		o
1000R-1	II		o												o	o	o		o			o	o	o
1002R	II		o				o									o						o	o	
11232 D1684	II		o				o						o			o			o			o		

* See text for further details.
** In bold the symbol used in Figs. 2-7. See Table S1 for complete list of minerals cited in the text.
*** Stolzite-rich composition (see text).

This is the peer-reviewed, final accepted version for American Mineralogist, published by the Mineralogical Society of America.
The published version is subject to change. Cite as Authors (Year) Title. American Mineralogist, in press.
DOI: https://doi.org/10.2138/am-2023-9126. http://www.minsocam.org/

Table 3
Grouping spectra in the two different spectral regions (see text).

	400 – 1800 cm^{-1}				2000 – 4000 cm^{-1}				
Type	I	II	III	IV	A	B	C	D	Ungrouped[§]
	C5	$P9_{yellow}$	$P9_{green}$	P18p	$P9_{yellow}$	$P18_{green}$	C26	902R	C5
	C26	902R	$P18_{yellow}$	911R-a	P18p	$P18_{yellow}$	911R-T	911R-g	$P9_{green}$
Samples*	$P18_{green}$	1002R	911R-g	912R	912R	990R		911R-a	997R
	911R-T		998R	990R	1000R	998R			
	997R			1000R		1002R			

* See Analytical methods for sample labels explanation.
§ Ungrouped: single spectra that cannot be grouped.

This is the peer-reviewed, final accepted version for American Mineralogist, published by the Mineralogical Society of America.
The published version is subject to change. Cite as Authors (Year) Title. American Mineralogist, in press.
DOI: https://doi.org/10.2138/am-2023-9126. http://www.minsocam.org/

Table 4
Bands assignments in the 400 – 1800 cm^{-1} spectral range for Types I-IV described in Table 3 (mineral symbols as in Table 1).

Type I		**Type II**		**Type III**		**Type IV**	
1624	Vbo/Ccl	1624	Vbo	1624	Vbo/Ccl	1624	Vbo/Ccl
1522	Mlc/Azu	1093	Ata/Vbo	1092	Ata/Vbo	1321	
1498	Mlc/Azu	1047	Ata	1026	Vbo/Ccl	1093	Ata/Vbo
1419	Mlc/Azu	1022	Vbo/Ata	856	Blk/Mott	1045	Ata
1400	Mlc/Azu	897	Ata/Vbo	820	Blk/Ata	1026	Vbo
1097	Mlc/Azu	841	Ata/Vbo	787	Blk/Vbo	989	Ata
1049	Mlc/Azu	781	Vbo	742	Mott/Vbo	928	Ata
987	Ata	766	Vbo	706	Blk	910	Ata
955	Azu/Ata	604	Ata	605	Ata	863	Ata
883	Ata/Azu	577	Ata	528	Blk/Vbo	847	Ata/Vbo
820	Ata/Azu	519	Ata/Blk	520	Blk/Ata	825	Ata
752	Mlc	434	Ata	505	Blk	769	Vbo
584	Mlc			453	Blk	735	Mott/Vna
524	Mlc			428	Blk	712	Mott
505	Mlc					669	Gp/Ccl
430	Mlc					602	Gp/Ata
						577	Ata
						517	Ata
						461	Vbo/Gp
						437	Ata

Ref. for bands assignments:
Vbo: Brown and Ross, 1972; Busca et al., 1994; Frost et al., 2011; Chukanov, 2014; Arvind et al., 2016; Bayat et al., 2018;
Ccl: Chukhrov et al.,1969; Frost and Xi, 2013; Chukanov, 2014.
Mlc/Azu: Goldsmith and Ross, 1968; Schmidt and Lutz, 1993; Frost et al., 2002b; Stoilova et al., 2002; Chukanov, 2014; Gao and Yuan, 2020;
Ata: Frost et al., 2002a; Martens et al., 2003; Tao et al., 2011; Chukanov, 2014.
Blk: Liu et al., 2011; Chukanov, 2014; Zhao et al., 2020.
Mott: Von Raden and Dicks, 1967; Frost et al., 2001; Chukanov, 2014; Frost et al., 2014.
Gp: Hass and Sutherland, 1956; Ross, 1974; Zapol' and Alksnis, 1977; Takahashi et al., 1983; Anbalagan et al., 2009; Bishop et al., 2014; Chukanov, 2014.

This is the peer-reviewed, final accepted version for American Mineralogist, published by the Mineralogical Society of America.
The published version is subject to change. Cite as Authors (Year) Title. American Mineralogist, in press.
DOI: https://doi.org/10.2138/am-2023-9126. http://www.minsocam.org/

Table 5
Bands assignments in the 3000 – 4000 cm^{-1} spectral range (see text for explanation).

Type A		**Type B**		**Type C**		**Type D**			**Ungrouped**		
						902R	911R-g	911R-a	997R	$P9_{green}$	C5
3448	Ata	3448	Ata	3425	Azu	3465			3442	3512	3428
3356	Ata	3423	Ata	3413	Azu/Mlc				3408	3428	
3334	Ata	3356	Ata	3363	Ata				3330	3413	
3319	Ata/Mlc	3340	Ata	3321	Ata/Mlc					3359	
		3330	Ata								

Ref. for bands assignments:
Ata: Frost et al. (2002); Martens et al. (2003); Tao et al. (2011); Chukanov (2014).
Mlc/Azu: Goldsmith and Ross (1968); Schmidt and Lutz (1993); Frost et al. (2002b); Stoilova et al. (2002); Chukanov (2014); Gao and Yuan (2020).
Blk: Liu et al. (2011); Chukanov (2014); Zhao et al. (2020).